Neuron

Article

Colocalization of different neurotransmitter transporters on synaptic vesicles is sparse except for VGLUT1 and ZnT3

Graphical abstract

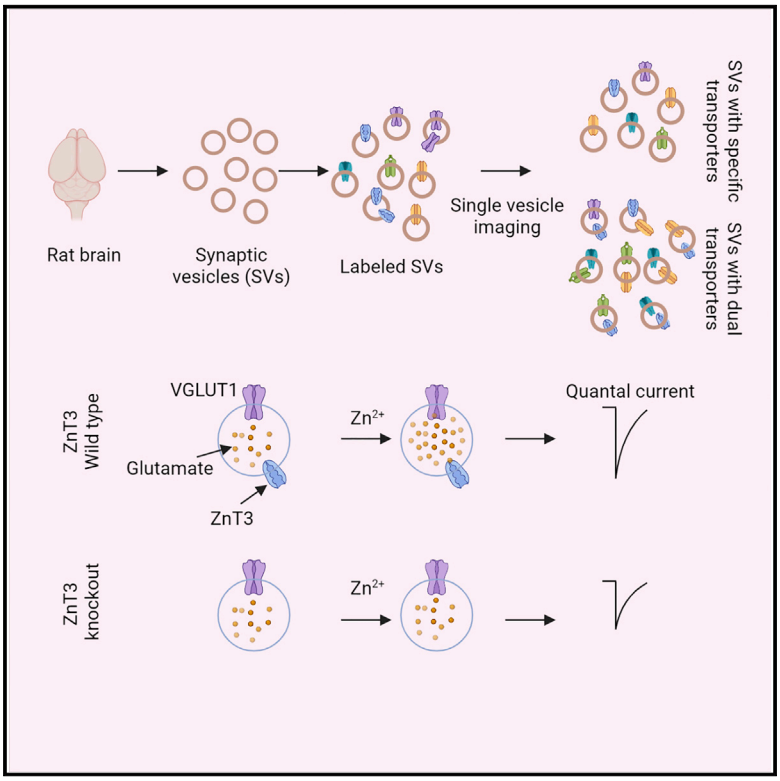

Highlights

- The majority of synaptic vesicles are specific for a single type of neurotransmitter
- Multi-transmitter vesicles are diverse and specific for distinct neurotransmitters
- The largest vesicle population carries two transporters, VGLUT1 and ZnT3
- Zinc facilitates vesicular glutamate content and quantal size via ZnT3

Authors

Neha Upmanyu, Jialin Jin, Henrik von der Emde, ..., Stefan W. Hell, Reinhard Jahn, Sivakumar Sambandan

Correspondence

siva.sambandan@mpinat.mpg.de

In brief

Specific neurons in the brain release more than one neurotransmitter. Upmanyu et al. show that a heterogeneous population of synaptic vesicles (SVs) are capable of releasing multiple transmitters, although the vast majority of SVs are specific for a single type of neurotransmitter.

Upmanyu et al., 2022, Neuron *110*, 1483–1497
May 4, 2022
https://doi.org/10.1016/j.neuron.2022.02.008

CellPress

Neuron

CellPress
OPEN ACCESS

Article

Colocalization of different neurotransmitter transporters on synaptic vesicles is sparse except for VGLUT1 and ZnT3

Neha Upmanyu,[1,2] Jialin Jin,[3] Henrik von der Emde,[4] Marcelo Ganzella,[2] Leon Bösche,[1,2] Viveka Nand Malviya,[2] Evi Zhuleku,[2] Antonio Zaccaria Politi,[5] Momchil Ninov,[6,7] Ivan Silbern,[6,7] Marcel Leutenegger,[4] Henning Urlaub,[6,7] Dietmar Riedel,[8] Julia Preobraschenski,[2,9,10] Ira Milosevic,[11,12] Stefan W. Hell,[4,13] Reinhard Jahn,[2] and Sivakumar Sambandan[1,2,4,14,*]

[1]Synaptic Metal Ion Dynamics and Signaling, Max Planck Institute for Multidisciplinary Sciences, Göttingen 37077, Germany
[2]Laboratory of Neurobiology, Max Planck Institute for Multidisciplinary Sciences, Göttingen 37077, Germany
[3]European Neurosciences Institute, A Joint Initiative of the University Medical Center Göttingen and the Max Planck Society, Göttingen 37077, Germany
[4]Department of NanoBiophotonics, Max Planck Institute for Multidisciplinary Sciences, Göttingen 37077, Germany
[5]Live-Cell Imaging Facility, Max Planck Institute for Multidisciplinary Sciences, Göttingen 37077, Germany
[6]Bioanalytical Mass Spectrometry, Max Planck Institute for Multidisciplinary Sciences, Göttingen 37077, Germany
[7]Institute of Clinical Chemistry, University Medical Center Göttingen, Göttingen 37075, Germany
[8]Department of Structural Dynamics, Max Planck Institute for Multidisciplinary Sciences, Göttingen 37077, Germany
[9]Institute for Auditory Neuroscience, University Medical Center Göttingen, Göttingen 37075, Germany
[10]Cluster of Excellence "Multiscale Bioimaging: from Molecular Machines to Networks of Excitable Cells" (MBExC), University of Göttingen, Göttingen 37075, Germany
[11]Wellcome Centre for Human Genetics, Nuffield Department of Medicine, NIHR Oxford Biomedical Research Centre, University of Oxford, Oxford OX3 7BN, UK
[12]Multidisciplinary Institute of Ageing, MIA-Portugal, University of Coimbra, Coimbra 3000-370, Portugal
[13]Department of Optical Nanoscopy, Max Planck Institute for Medical Research, Heidelberg 69028, Germany
[14]Lead contact
*Correspondence: siva.sambandan@mpinat.mpg.de
https://doi.org/10.1016/j.neuron.2022.02.008

SUMMARY

Vesicular transporters (VTs) define the type of neurotransmitter that synaptic vesicles (SVs) store and release. While certain mammalian neurons release multiple transmitters, it is not clear whether the release occurs from the same or distinct vesicle pools at the synapse. Using quantitative single-vesicle imaging, we show that a vast majority of SVs in the rodent brain contain only one type of VT, indicating specificity for a single neurotransmitter. Interestingly, SVs containing dual transporters are highly diverse (27 types) but small in proportion (2% of all SVs), excluding the largest pool that carries VGLUT1 and ZnT3 (34%). Using VGLUT1-ZnT3 SVs, we demonstrate that the transporter colocalization influences the SV content and synaptic quantal size. Thus, the presence of diverse transporters on the same vesicle is bona fide, and depending on the VT types, this may act to regulate neurotransmitter type, content, and release in space and time.

INTRODUCTION

Synaptic vesicles (SVs) are the trafficking organelles responsible for storage and release of various neurotransmitters at the synapse, with the type and content of the transmitters determined by the presence of specific vesicular transporters (VTs). Although a given neuron is thought to release only one type of neurotransmitter (referred as Dale's principle), it is well established that certain neurons in the vertebrate central nervous system (CNS) release more than one classical (non-peptide) neurotransmitter upon activation, referred as "cotransmission" (Hnasko and Edwards, 2012; Tritsch et al., 2016; Trudeau and El Mestikawy, 2018; Vaaga et al., 2014). Recent evidences demonstrate that specific neurons release multiple transmitters from the same synapse (Ren et al., 2011; Shabel et al., 2014; Varga et al., 2009). While the prevalence and the physiological role of such pluralism is not clear, it has also been difficult to ascertain whether the release of multiple neurotransmitters occurs from the same (referred as "corelease") or different pools of vesicles that may exhibit differential calcium sensitivity. This knowledge is crucial for the understanding of synaptic function and computation.

Corelease of distinct neurotransmitters from the same SVs requires that the respective vesicles contain the corresponding

VTs, but the available information is not sufficient to confirm the same. For both corelease and cotransmission, the VTs must be co-expressed in the neurons. A recent large-scale single-cell transcriptomics study (involving ~70,000 neurons) of the CNS revealed that roughly 5% of neurons co-express multiple VTs, indicating the capacity for cotransmission or corelease (Zeisel et al., 2018). Further analysis of the data reveals that the multi-transporter neurons are highly diverse, expressing up to four different transporters, implying an unappreciated complexity of synaptic signaling (Figure S1). Considering the limitations in transcript detection in single-cell studies, it is conceivable that the actual population of neurons expressing multiple VTs may be higher, hinting at widespread cotransmission or corelease in the brain.

Recent discoveries using optogenetics, *in vivo* electrophysiology, and anatomical approaches, have convincingly established the identity of an array of dual transmitter neurons and their postsynaptic partners in specific brain regions (Ren et al., 2011; Shabel et al., 2014; Takács et al., 2018; Varga et al., 2009). The two major fast neurotransmitters, glutamate and GABA, have been shown to be released together with another transmitter that is of modulatory nature. For example, glutamate is released together with dopamine in the striatum and the ventral tegmental area (VTA) (Chuhma et al., 2014; Hnasko et al., 2010; Stuber et al., 2010), or with serotonin in the hippocampal raphe nuclei projections (Sengupta et al., 2017; Varga et al., 2009), or with acetylcholine in striatal interneurons and medial habenula projections (Frahm et al., 2015; Gras et al., 2008; Higley et al., 2011; Ren et al., 2011). Similarly, GABA is cotransmitted with acetylcholine in basal forebrain projections (Saunders et al., 2015; Takács et al., 2018), or with dopamine in the olfactory bulb (Liu et al., 2013) and the striatum (Tritsch et al., 2012). Interestingly, cotransmission of glutamate and GABA has also been observed in some neurons (Root et al., 2018; Shabel et al., 2014), including evidence for their corelease (Shabel et al., 2014). Despite this considerable progress, a compilation of recent studies on multi-transmitter neurons (Table S1) reveals that only a few examples exist to corroborate, corelease, or co-localize transporters on the same vesicle (Fasano et al., 2017; Root et al., 2018; Saunders et al., 2015; Takács et al., 2018; Zimmermann et al., 2015). Immunogold electron microscopy (IEM) following dual labeling of colocalized transporters provides an indication for corelease (Takács et al., 2018; Zander et al., 2010) but it may not provide quantitative information due to the limited sensitivity of IEM. Electrophysiological recordings of dual transmitter responses following optogenetic stimulations can only indicate, but not conclude, corelease and can only be applied to the study of specific pre-post neuronal populations (Shabel et al., 2014; Takács et al., 2018). Functional *in vitro* and biochemical experiments such as measuring the effect of one transmitter on the vesicular uptake of the other (Gras et al., 2008) or SV immunoisolation (Grønborg et al., 2010) goes one notch up to explore the corelease of transmitters. Nonetheless, these are bulk experiments that could lead to false-positive vesicular colocalization. Thus, the above approaches, when applied either individually or together, yield a wealth of information on dual transmitter signaling but are inadequate to confirm corelease and do not address the extent of the phenomenon in the whole mammalian brain.

In this study, we visualized different VTs at the single-vesicle level, resulting in a comprehensive and quantitative colocalization map of transporters and revealing the extent and diversity of corelease in the adult rodent brain. We have also studied one example of corelease to understand the benefits and relevance for synaptic physiology.

RESULTS

DyMIN STED allows high-throughput super-resolved imaging of single SVs in association with an enhanced fluorescence signal

Dynamic minimum stimulated emission depletion (DyMIN STED) nanoscopy, a recently developed super-resolution microscopy technique that provides super resolution with efficient fluorescence detection, was used to image single SVs derived from rat brain. DyMIN STED modulates the power of the depletion light depending on the local brightness in the sample, in contrast to conventional STED microscopy that applies maximum STED laser power throughout the imaging area (Göttfert et al., 2017; Heine et al., 2017). Thus, the overall light exposure of the sample is reduced, leading to decreased photobleaching and an enhanced fluorescence signal from single vesicles (Figures 1A–1C). In contrast to conventional high-resolution microscopy (Farsi et al., 2016), DyMIN STED significantly improved the resolution of single labeled vesicles (Figure 1B). The average size of individual SVs labeled for Synaptobrevin2 (Syb2), measured in terms of the standard deviation (SD) of an integrated Gaussian fit (σ) on each puncta in DyMIN STED, was ~33 nm, as expected for the size of labeled SVs (Takamori et al., 2006) versus ~126 nm with confocal microscopy. Additionally, adapting the STED laser intensity to the fluorophore density improved the signal-to-noise ratio while maintaining the fluorescence signal similar to that of confocal microscopy (Figure 1B). To immunolabel SVs, we developed a strategy that maximized epitope coverage while effectively removing background fluorescence from unbound antibodies (Figure S2). Freshly isolated SVs of high purity (Takamori et al., 2006) were indirectly labeled using saturating concentrations of the antibody "in-solution," followed by an additional size exclusion chromatography (SEC) step to remove unbound antibodies. The above method significantly increased the fluorescence brightness of single vesicles when compared with the conventional labeling that is performed after surface immobilization of SVs (Figure 1D). The enhanced epitope coverage through "in-solution" labeling is particularly favorable for targets with a limited fluorescence budget such as VTs (Figure 1E). In addition, negative controls using samples that lacked either SVs or the primary antibody exhibited insignificant background fluorescence (~0.1%; Figures S3A–S3C), which has been accounted for in all further quantitative analyses. The combination of DyMIN STED and the labeling protocol thus allowed high-throughput visualization of super-resolved SVs for quantitative fluorescence analysis.

Two-color DyMIN STED reveals the colocalization pattern of diverse transporters on the same vesicle

Two-color DyMIN STED imaging of Synaptophysin (Syp), a marker present on all SVs irrespective of the neurotransmitter

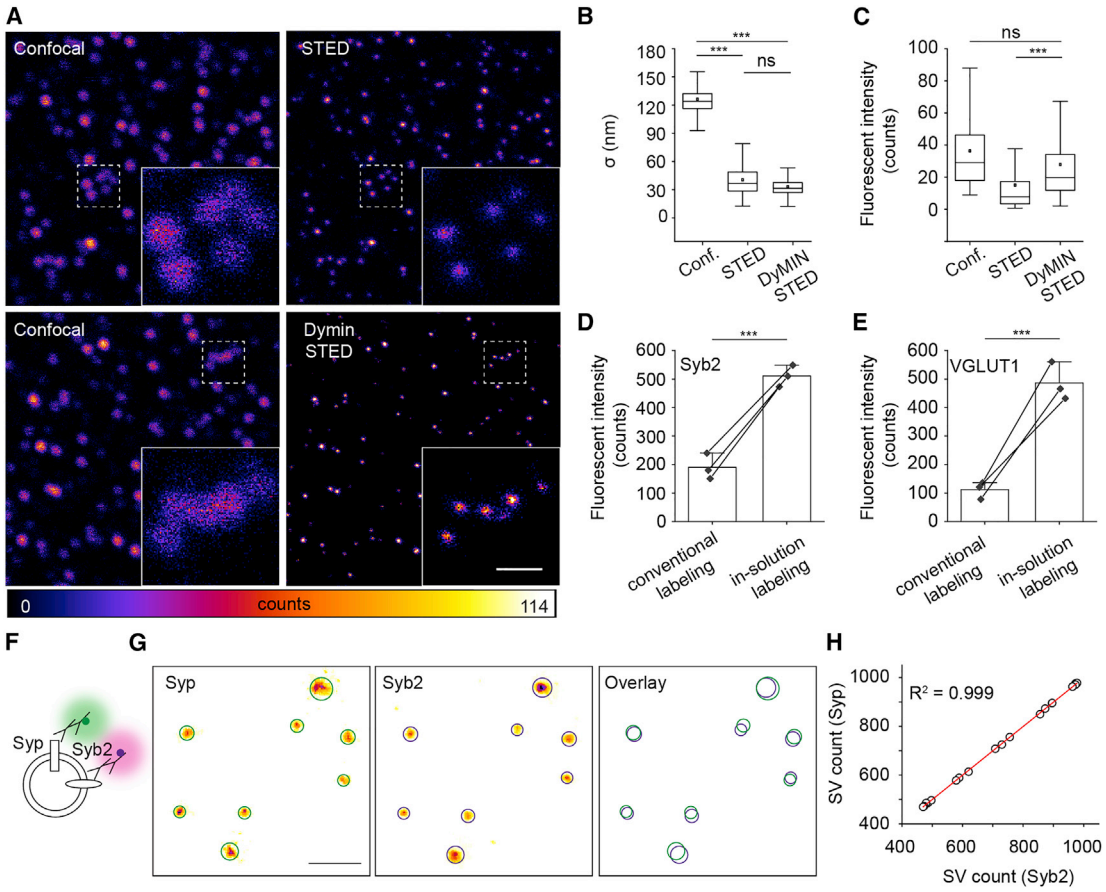

Figure 1. DyMIN STED allows high-throughput super-resolved imaging of "in-solution" labeled single SVs in association with enhanced fluorescence retention

(A) Representative images of Synaptobrevin2 (Syb2) labeled SVs in confocal, conventional, and DyMIN STED mode. Insets are magnified regions marked in dashed white squares, showing putative single vesicles in the confocal that are clearl y resolved into multiple vesicles in the conventional and DyMIN STED. Scale bar, 500 nm.

(B) Boxplot showing a significant increase in the spatial resolution of single vesicles in the conventional and DyMIN STED mode in comparison with the confocal mode. Box range represents 25th–75th percentile, and the whiskers represent outliers (***$p < 0.01$; unpaired t test, n = 3).

(C) Boxplot showing comparable fluorescence intensity of individual vesicles between confocal and DyMIN STED, indicating reduced photobleaching caused by STED light. Box range represents 25th–75th percentile, and the whiskers represent outliers ($p = 1.74$, not significant between confocal and DyMIN STED; ***$p < 0.01$, between conventional and DyMIN STED; unpaired t test; n = 3).

(D and E) Bar graphs showing a significant increase in fluorescence intensity when vesicles were labeled "in-solution" in comparison with the conventional labeling following surface immobilization of SVs. Error bars represent SEM (***$p < 0.01$; unpaired t test, n = 3). Note that there is ~5-fold increase in the fluorescence intensity when SVs were labeled for VGLUT1 compared with ~2.5-fold increase for Syb2, indicating enhanced epitope coverage for proteins with low copy numbers such as VGLUT1.

(F) Illustration depicting double immunolabeling of purified SVs against Synaptophysin (Syp) and Syb2 using two spectrally distinct fluorescent dyes.

(G) Representative two-color DyMIN STED images (inverse color map) of SVs for Syp and Syb2. Green and magenta circles portray the SV area derived by a 2D Gaussian fit on Syp and Syb2 puncta, respectively. The overlay of the merged circle profiles from the two channels shows the complete overlap of all Syp and Syb2 puncta. Scale bar, 500 nm.

(H) Scatter plot of the detected Syp and Syb2 puncta count in different experiments. Linear regression of the data shows even distribution of Syp and Syb2 (n = 4 experiments, >14,000 SVs for both channels). See also Figures S2–S4.

phenotype (Takamori et al., 2000; Figure S4), and Syb2 showed colocalization of nearly all puncta in both channels, revealing that both Syp and Syb2 act as a marker for the total number of SVs (Figures 1F–1H). Colocalization was determined using a co-ordinate-based colocalization analysis (Malkusch et al., 2012; Figures S4 and S5; STAR Methods) since the SV puncta followed a Rayleigh distribution as described in previous reports (Geumann et al., 2008). To determine the proportion of SVs expressing a given transporter within the total SV population, we performed dual immunolabeling of SVs for Syp and each of the following VTs: VGLUT1, VGLUT2, VGLUT3 (specific for glutamate), VGAT (specific for GABA and Glycine), VMAT2 (specific for monoamine transmitters), VAChT (specific for acetylcholine), and ZnT3 (specific for Zn^{2+}). VGLUT1, VGLUT2, and VGLUT3 were detected on approximately 60%, 23%, and 2.8% of all SVs, respectively, in agreement with previous reports (Takamori

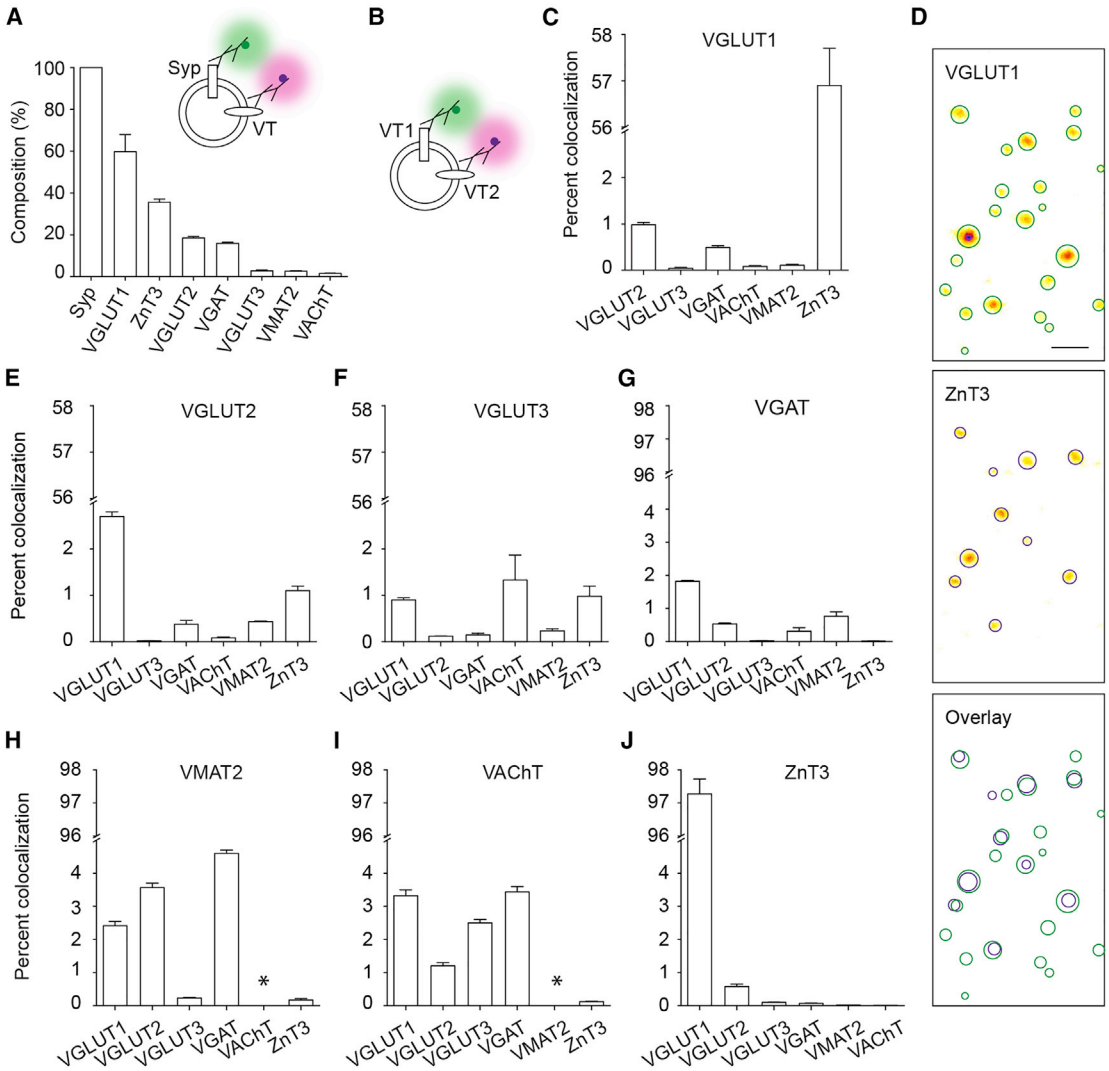

Figure 2. Two-color DyMIN STED reveals the colocalization pattern of diverse transporters on the same vesicle

(A) Bar graph quantifying the proportion of SVs expressing a specific VT. Values are normalized to Syp, which acted as the reference for total SVs. The inset illustrates double immunolabeling of SVs against Syp and a VT. Error bars represent SEM (n = 3 experiments for each pair; >10,000 total SVs for each dual labeling).

(B) Illustration depicting dual immunolabeling of SVs against two different VTs (VT1 and VT2).

(C) Bar graph showing the degree of vesicular colocalization of VGLUT1 against the specific VTs on the x axis. Error bars represent SEM (n > 3 experiments for each pair; >10,000 total SVs for each dual labeling).

(D) Representative images (inverse color map) of VGLUT1 and ZnT3 channels from the two-color DyMIN STED experiment shown in (C). Circles portray the SV area derived by a 2D Gaussian fit on VGLUT1 (green) and ZnT3 (magenta) puncta. The overlay shows merged SV circle profiles of the two channels (n > 3 experiments; >20,000 total SVs for both VGLUT1 and ZnT3). Scale bar, 200 nm.

(E–J) Bar graphs showing the degree of vesicular colocalization of a specific VT indicated on top of each graph against the VTs on the x axis (n = 3 experiments for each pair; >10,000 total SVs for each dual labeling). No data are shown for the VMAT2 and VAChT combination. All values are means ± SEM. See also Figures S3–S6.

et al., 2006; Wilhelm et al., 2014; Figure 2A). VGAT labeling was detected on 15.9% of all SVs, again confirming earlier reports (Takamori et al., 2006, 2000). VMAT2 and VAChT were present on 2.6% and 1.5% of SVs, respectively (Figure 2A). Surprisingly, ZnT3 was detected in a large population of SVs; a staggering ~30% of all SVs were ZnT3-positive (Figure 2A). Although the VT antibodies used above have been well characterized (Gras et al., 2008; Herzog et al., 2006; Hnasko et al., 2010; Takamori et al., 2000), we tested their specificity for single-vesicle imaging using purified chromaffin granules (CG; Figure S3D), which share many proteins with SVs including the fusion machinery but lack the above VTs. None of the VT antibodies resulted in staining, confirming their high specificity (Figure S3). The marginal background fluorescence primarily due to secondary antibodies (~0.1%) was accounted for in all single-vesicle quantifications.

To investigate the expression of multiple VTs on the same vesicle, we measured the degree of colocalization between two distinct transporters in all possible pairwise combinations using two-color DyMIN STED microscopy (Figures 2B–2J). For glutamatergic vesicles (excitatory), interesting differences became apparent when comparing the three VGLUT isoforms (VGLUT-1–3). First, the overlap between the two abundant variants, VGLUT1 and VGLUT2, was low (Figures 2H and 2I; ~1% of VGLUT1 SVs contain VGLUT2), in contrast to their coexistence during development (Herzog et al., 2006) but in agreement with the non-overlapping expression pattern of the two VTs in adulthood (El Mestikawy et al., 2011; Takamori et al., 2001). Second, while VGLUT2 did not show any preference to dopaminergic or cholinergic vesicles, VGLUT3 showed preference to VAChT (Figures 2E and 2F). In contrast, VMAT2 showed preference to VGLUT2 whereas VAChT showed no such preference to any VGLUTs (Figures 2H and 2I). Co-expression of the above VTs was previously observed in dopaminergic and cholinergic neurons in the midbrain and the striatum (Gras et al., 2008; Hnasko et al., 2010). Third, VGLUT1 but not the two other variants showed colocalization preference with ZnT3 (~57%; Figures 2C–2E and 2J). We confirmed the robust colocalization of ZnT3 and VGLUT1 in SV preparations from mice using three different antibodies of ZnT3, for which specificity was validated by western blot or single-vesicle imaging in ZnT3 knockout mice (KO; Cole et al., 1999; Figure S6).

VGAT, the transporter defining GABAergic vesicles, was shown previously to be colocalized with other VTs at many synapses (Tritsch et al., 2016). However, on the vesicle level, VGAT shows marginal overlap with other VTs. For instance, VMAT2 and VAChT are only found on ~0.75% and ~0.3% of GABAergic vesicles, respectively (Figure 2G), suggesting that corelease of GABA with monoamines or acetylcholine from the same vesicle pool is not widespread. On the contrary, both monoaminergic and cholinergic SVs generally showed marginal degrees of colocalization with VGLUTs and VGAT (Figures 2H and 2I, note that colocalization between VMAT2 and VAChT could not be measured; STAR Methods). Finally, we also examined SVs that carry one of the VGLUT variants and VGAT. Both VGLUT1 and VGLUT2 showed similar levels of colocalization with VGAT (slightly below 0.5%). Overall, VTs exhibit a diverse combination of colocalization on single SVs.

SVs are highly diverse, based on the phenotype of expressed vesicular transporters

The above colocalization pattern of VTs and the proportion of SVs carrying a specific VT in the entire SV population allowed us to quantify the relative abundance of SVs carrying a specific VT phenotype. (Figures 3A and 3B). We identified 27 classes of SVs, each carrying either one or two distinct VTs (Figure 3A). Interestingly, the SV classes sum up to ~102%, indicating coverage of the total SV population by the labeling method. The fraction of SVs specific for a single neurotransmitter (i.e., carrying only one VT) is ~64%, suggesting that roughly one-third of SVs are capable of storing more than one neurotransmitter. The multi-transmitter SV population, however, is predominantly represented by the VGLUT1-ZnT3 vesicle, which accounts for ~34% of all SVs. To validate the high degree of colocalization between VGLUT1 and ZnT3, we performed IEM on isolated rat SVs (Figure 3A, inset; see STAR Methods). Indeed, a modest population of SVs was positive for both VGLUT1 and ZnT3, in spite of the lower sensitivity of IEM when compared with light microscopy.

We also determined the composition of excitatory SVs, characterized by the expression of either one of the three VGLUT subtypes (VGLUTs) or in combination with another VT (Figure 3C). While a variety of excitatory SVs involving different combinations of VGLUTs and other transporters exist, two defining features are very conspicuous—(1) the sheer abundance of VGLUT1-ZnT3 SVs (~42% of excitatory SVs), which we will focus on in the later sections, and that (2) only ~0.7% of the excitatory SVs carry both VGLUT1 and VGLUT2. The low overlap between VGLUT1 and VGLUT2, in spite of their co-expression during early development stages (Herzog et al., 2006), reflects a near-complete replacement of VGLUT1 for VGLUT2 in the adult cortex.

Inhibitory SV composition, characterized by the expression of only VGAT or in combination with another VT, has also been deduced (Figure 3D). Interestingly, only 3.5% of VGAT-positive SVs carry another transporter, which was not anticipated in view of the increasing evidence for cotransmission of GABA together with other neurotransmitters (Tritsch et al., 2016), suggesting that VGAT and other VTs exist in segregated pools at those synapses. A very small population of GABA-glutamatergic SVs (~0.37% of all SVs) have also been detected carrying VGAT and one of the VGLUT subtypes. Interestingly, the composition of GABA-glutamatergic SVs also provides some insight into the VGLUT subtype that is majorly involved in GABA corelease (Figure 3E). Among the three subtypes, VGLUT1 is preferentially colocalized with VGAT, although only VGLUT2 has been predominantly detected for corelease of glutamate with GABA (Shabel et al., 2014).

Taken together, the SVs carrying two VTs are highly diverse although the overall degree of colocalization between any transporter pair is low (consistently below 5% of all SVs), which is in agreement with the abundance of neurons capable of releasing more than one neurotransmitter (Figure S1). Thus, a vast majority of all SVs are indeed specific for only a single neurotransmitter, with the exception of VGLUT1-ZnT3 SVs.

ZnT3 is a highly abundant SV protein with ~4 copies per vesicle

The high degree of colocalization between VGLUT1 and ZnT3 prompted us to examine ZnT3 protein abundance, expression, and distribution. First, we measured the amount of ZnT3 protein in SVs with quantitative immunoblotting using highly purified recombinant ZnT3 protein (42 kDa) as a standard (Figures 4A and 4B). Increasing amounts of SVs and purified ZnT3 were loaded on the same gel and ZnT3 was detected using a specific monoclonal antibody (Figure 4A). The amount of ZnT3 in the SVs, obtained from the standard curve, was ~12 ng/μg of SVs (Figure 4B; 262 ± 23 fmol/μg of SVs), revealing that ZnT3 is one of the most abundant SV membrane proteins (~1.5% of the total amount of SV proteins; see Takamori et al., 2006). Next, we performed quantitative mass spectrometry (MS) of the SV proteome using a label-free intensity-based absolute quantification (iBAQ) approach (Figure 4C). We detected ~1,500 proteins, including

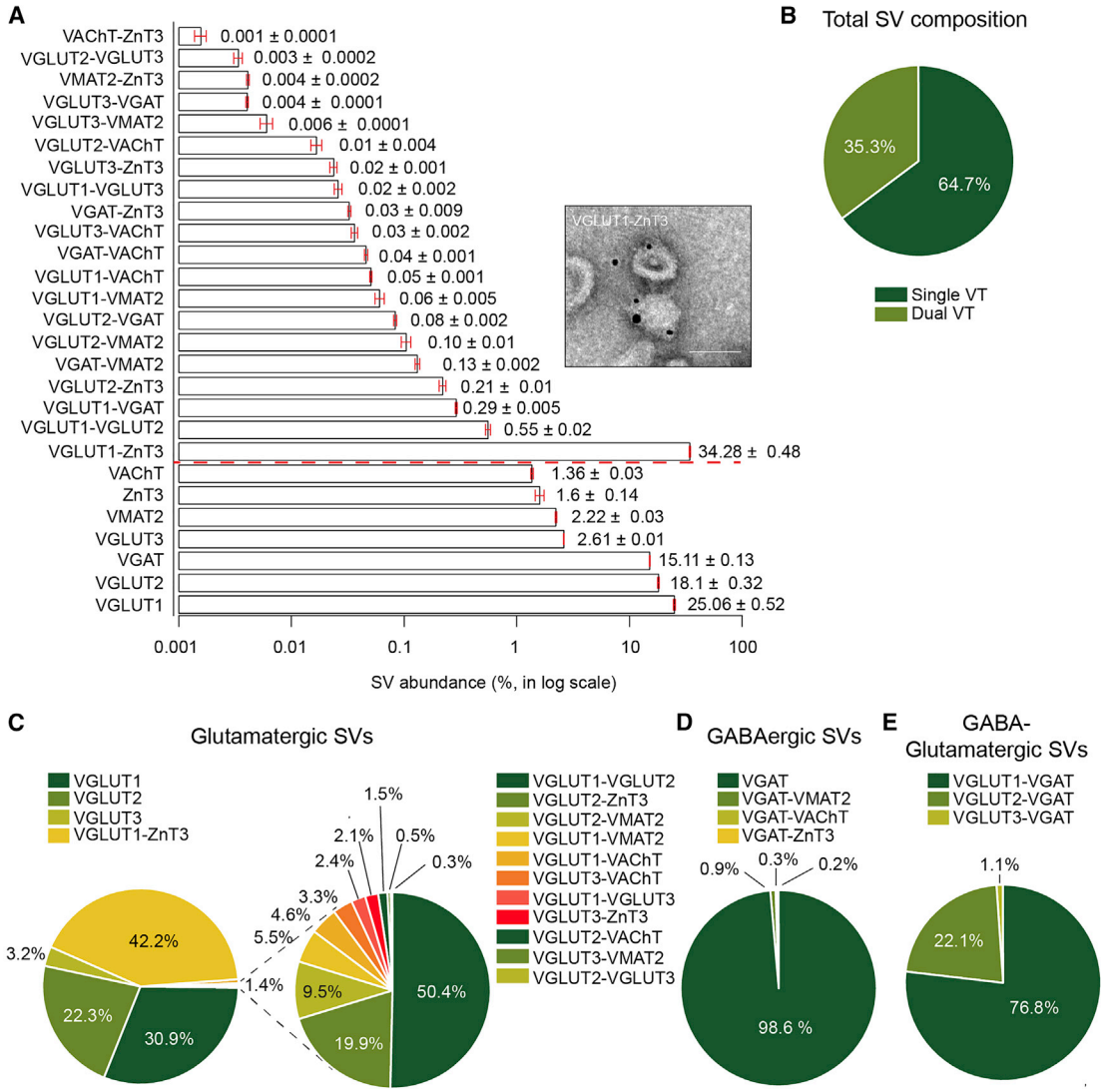

Figure 3. SVs are highly diverse, based on the phenotype of expressed vesicular transporters

(A) Bar graph showing the relative abundance of different vesicle classes containing either one (below dashed red line) or two (above the red dashed line) distinct VTs, obtained from the colocalization degree of each VT pair and the respective proportion of each VT in the total SV pool as shown in Figure 2. The numbers next to each bar denotes the actual value. Inset: representative electron immunogold microscopy (IEM) image validating colocalization of VGLUT1 and ZnT3 by displaying gold nano-particles specific for VGLUT1 (5 nm) and ZnT3 (10 nm) (n = 2 IEM experiments, 4.14% of all SVs carried gold particles specific for both VGLUT1 and ZnT3; 35.6% and 6.7% of vesicles were positive for VGLUT1 and ZnT3 alone; negative controls that lacked primary antibodies exhibited negligible signals). Bar graph values are means ± SEM. Scale bar in the inset, 50 nm.

(B) Pie diagram showing the broad composition of total SVs containing either one or two distinct VTs.

(C) Left, pie diagram showing the composition of glutamatergic vesicles expressing either one of the three vesicular glutamatergic transporters (VGLUT1-3) or in association with another VT. Right, the small components are visualized by an exploding pie chart recalibrated to 100% for greater visibility.

(D) Similar pie chart, as shown in (C), for GABAergic vesicles expressing VGAT.

(E) Similar pie chart, as shown in (C), for SVs expressing one of the three VGLUTs and VGAT. All statistics above were obtained from two-color DyMIN STED images. See also Figure S1.

low abundance transporters such as VMAT2 and VAChT, each with individual iBAQ values (Table S2). In agreement with immunoblotting measurements, ZnT3 was detected as an abundant SV protein with approximately one-third of the absolute amount of VGLUT1 (Figure 4C). To determine the copy number of ZnT3 per vesicle, we divided the number of molecules by the number of ZnT3-positive vesicles per μg of SVs (as given in Takamori et al., 2006 and Figure 2D). The average ZnT3 copy number was estimated to be roughly half of the average copy number of VGLUT1 (Figure 4C).

To directly measure the copy number of VGLUT1 and ZnT3 on individual SVs, we developed an imaging-based approach using DyMIN STED (Figures 4D–4F; see STAR Methods). Compared to MS estimates, (Takamori et al., 2006; Taoufiq et al., 2020), the

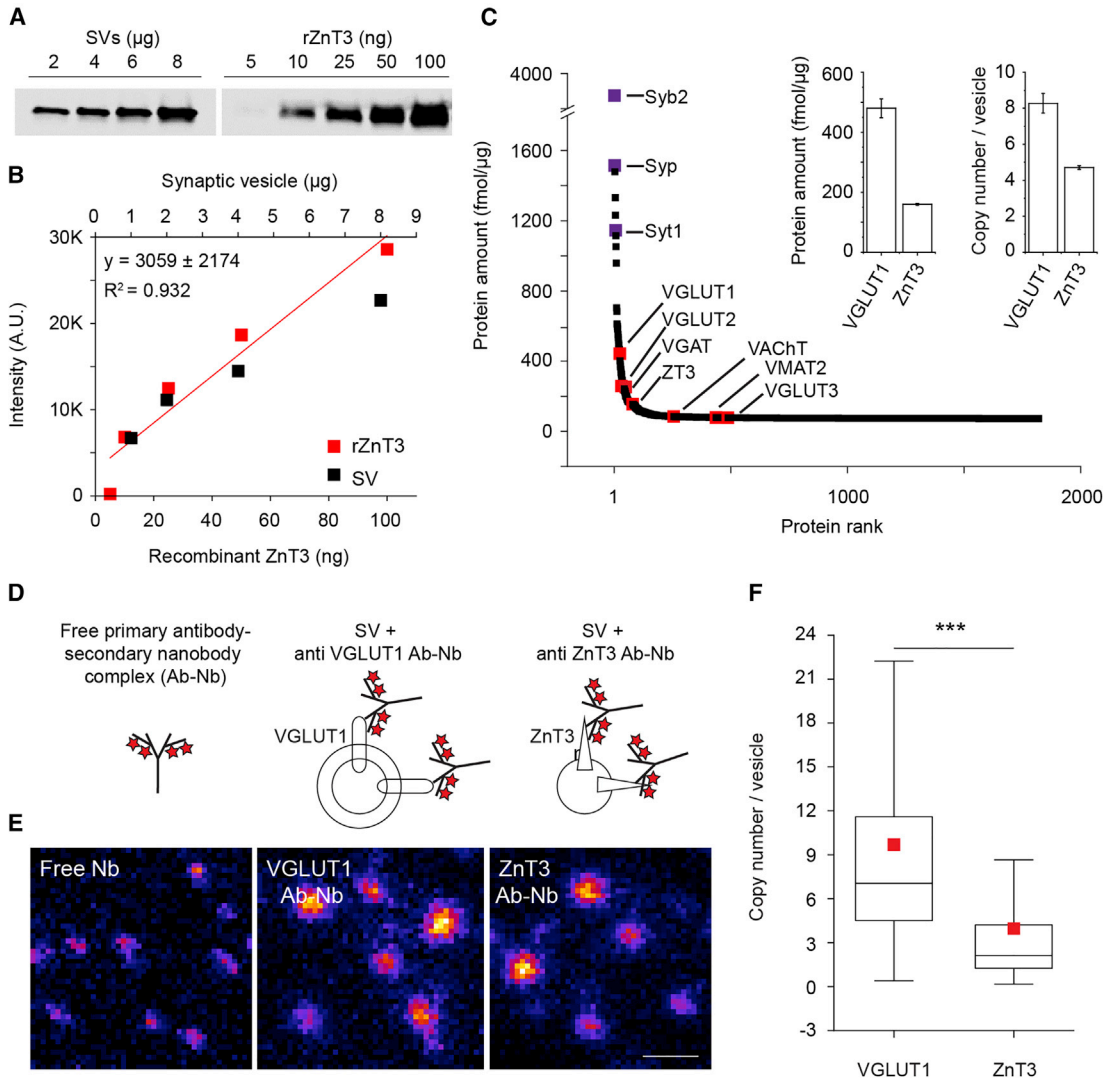

Figure 4. ZnT3 is a highly abundant SV protein, with ~4 copies per vesicle

(A) An example quantitative immunoblot for ZnT3 in SVs and purified recombinant ZnT3 protein (rZnT3, standard) at specified concentrations.

(B) Scatter plot showing the quantification of ZnT3 abundance in SVs using rZnT3 as standard (n = 2 biological samples).

(C) SV proteins ranked by their abundance, as estimated by quantitative mass spectrometry (MS). Selected SV proteins are color-coded for visibility; purple for specified SV markers (Syb2, Syp, and Syt1) and red for the specified VTs. Inset: bar graphs showing the relative abundance (left) and copy number (right) of VGLUT1 and ZnT3 estimated from MS analysis. Error bars represent SEM (n = 2 biological samples).

(D) Illustration of the labeling of purified SVs to determine the copy number of VGLUT1 and ZnT3 via single-vesicle imaging. The stoichiometric ratio between VGLUT1 (middle) or ZnT3 (right) molecules and the number of fluorophores was preserved using monoclonal primary antibody and secondary nanobody conjugated to a fixed number of fluorophores (Ab-Nb).

(E) Representative DyMIN STED images (fire) of free Ab-Nb (left) and SVs labeled against VGLUT1 (middle) and ZnT3 (right), as described above. Scale bar, 100 nm.

(F) Boxplot quantifying the copy numbers of VGLUT1 and ZnT3 in individual SVs. Box range represents 25th–75th percentile, and the whiskers represent outliers (n = 3, $p < 0.001$, unpaired t test).

single-vesicle imaging-based approach revealed the variability of copy numbers between the vesicles (Mutch et al., 2011). While both VGLUT1 and ZnT3 copy numbers exhibited high variability, the average copy number of ZnT3, in agreement with MS estimation, was lower than that of VGLUT1 (VGLUT1, 9.46 ± 0.06 [mean ± SEM], 7.96 [SD]; ZnT3, 3.63 ± 0.07 [mean ± SEM], 2.45 [SD]; Figure 4F).

Finally, we performed immunoisolation of ZnT3 SVs using a monoclonal anti-ZnT3 antibody and detected selected proteins through western blotting. As expected, ZnT3 immunoisolated SVs showed selective enrichment of VGLUT1 when compared with the control SVs that were immunoisolated using anti-syb2 antibody, representing all SVs (Figure S7). In addition to VGLUT1, another SV membrane protein, SV2B, was also

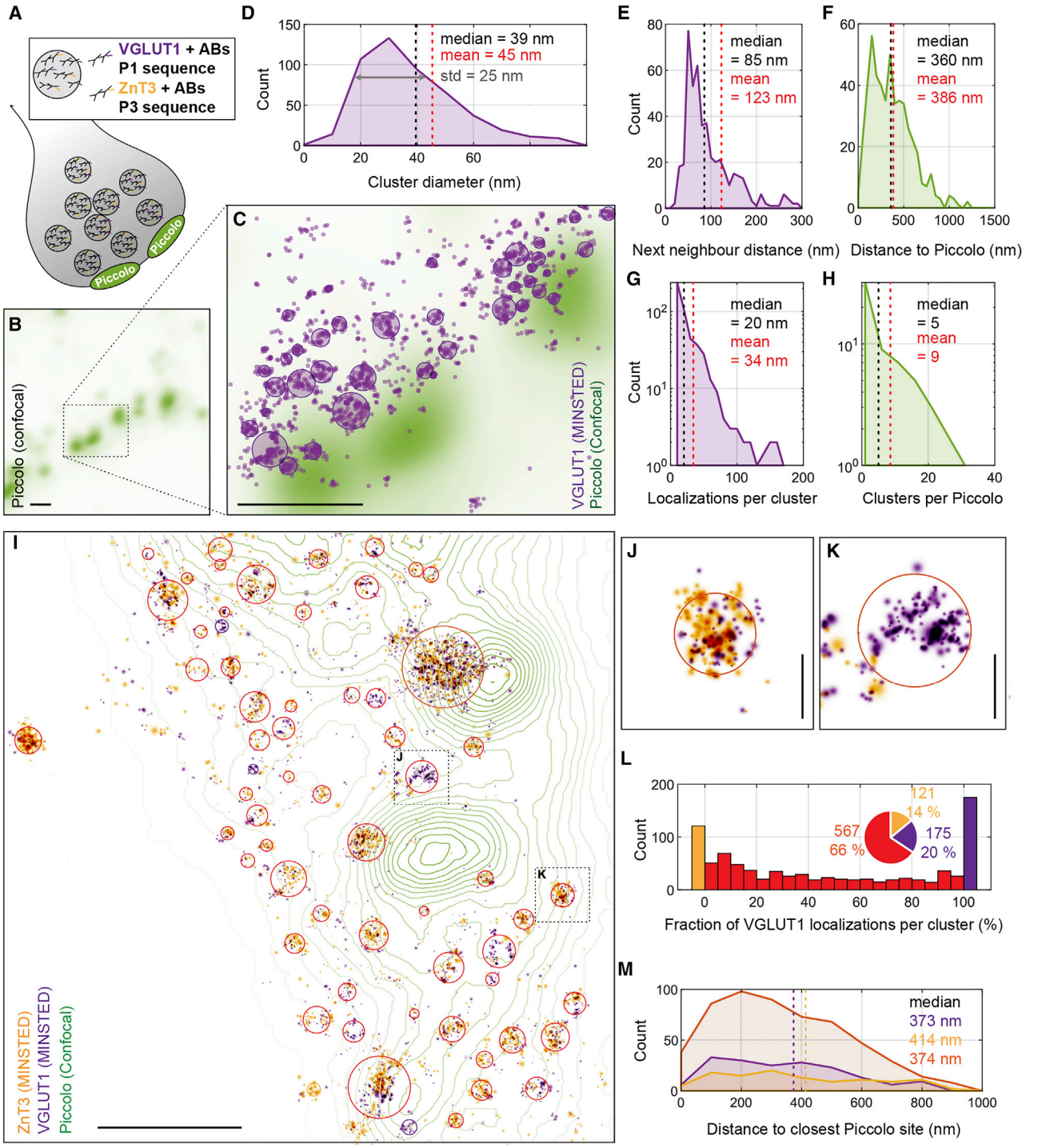

Figure 5. Heterogeneous pools of SVs containing VGLUT1, ZnT3, or VGLUT1-ZnT3 reside at individual synapses

(A) Illustration showing DNA PAINT labeling of VGLUT1 and ZnT3 with Piccolo as the AZ marker in hippocampal culture neurons.

(B) A representative confocal image of a selected synapse region showing the Piccolo distribution. Scale bar, 400 nm.

(C) An image of the zoomed-in region from (B) showing 2D MINSTED localization position estimates of VGLUT1 with Piccolo in green background. The purple circles represent the two-sigma range around the VGLUT1 cluster centers. Scale bar, 400 nm.

(D) Histogram showing the size distribution of VGLUT1 clusters.

(E) Lateral distance distribution of VGLUT1 clusters to their nearest neighbor.

(F) Lateral distance distribution of VGLUT1 clusters to their nearest AZ.

(legend continued on next page)

enriched in the ZnT3 immunoisolate, concurring with earlier findings in SVs immunoisolated with VGLUT1 antibodies (Grønborg et al., 2010). Overall, the above data reveal that ZnT3 is an abundant SV protein that is broadly expressed as an integral component of VGLUT1-containing SVs.

Heterogeneous pools of SVs containing VGLUT1, ZnT3, or VGLUT1-ZnT3 reside at individual synapses

VGLUT1 and ZnT3 exhibit an overlapping expression pattern on the mesoscale (McAllister and Dyck, 2017). To compare the synaptic distribution of the transporters, we labeled the proteins together with an active zone (AZ) marker, Piccolo, in cultured primary hippocampal neurons and visualized them using confocal microscopy. A pixel-based correlation revealed a high degree of overlap between both the transporters (Figures S6E and S6G), indicating that almost every VGLUT1 synapse is positive for ZnT3. To further probe the intrasynaptic distribution of VGLUT1 and ZnT3, we imaged individual synapses at single fluorophore level using 2D MINSTED nanoscopy (Figures 5A–5M) with DNA PAINT labeling. MINSTED is the most recent member of the STED family, carrying out the DyMIN STED principle on individual fluorophores with a highly efficient sampling algorithm and thus ultimately providing spatial resolution at the molecular scale (1–3 nm) (Weber et al., 2021). We imaged VGLUT1 and ZnT3 channels with MINSTED and Piccolo using confocal microscopy. Individual SVs were identified by cluster analysis of the binding events within the projection plane and characterization of the size of SVs, nearest neighbor distance, number of SVs per AZ, distance of the SVs to the AZ, and the number of binding events per SV was performed in 2D (Figures 5A–5H).

MINSTED DNA PAINT multiplexing directly revealed that ZnT3 and VGLUT1 colocalize on the same SVs at individual synapses (Figures 5I–5L). We visualized three different pools of SVs close to the manually selected AZs, carrying distinct VT types—only VGLUT1, only ZnT3, and VGLUT1-ZnT3. While, on average, there is no significant difference in the total number of vesicles positive for VGLUT1 or ZnT3 per synapse, vesicles carrying both the transporters accounted for roughly 66% of all SVs (Figure 5L). The large degree of colocalization could partly result from axial overlay of SVs or background events from either one of the proteins but, in general, it confirms the findings obtained from purified SVs (Figure 2C). We found no difference between the three different SV pools with their respective distances to AZ (Figure 5M). It should be kept in mind that the presence or the lack of differences in the lateral distances could be partially due to axially overlapping structures in 3D.

Zn^{2+} facilitates vesicular glutamate content by a mechanism mediated by ZnT3

Does the presence of an active Zn^{2+} transport affect glutamate transport activity? To address this issue, we measured the glutamate content of purified SVs from mice (LP2 fraction; Takamori et al., 2006) using a fluorescence-based *in vitro* assay (see STAR Methods and Preobraschenski et al., 2014). Vesicular glutamate uptake was performed in the presence of different concentrations of Zn^{2+} ($[Zn^{2+}]$) and, following the SV rupture, glutamate was detected using iGluSnFR, a protein-based glutamate sensor (Marvin et al., 2018; Figures 6A–6C). Glutamate uptake into vesicles was dose-dependently facilitated by Zn^{2+} and exhibited a maximal 2-fold increase with an EC50 of ~25 nM (Figures 6B and 6C), a physiologically relevant cytoplasmic $[Zn^{2+}]$ in the confined volume of a typical presynaptic compartment (3.7×10^{-22} L; Goch and Bal, 2020; Wilhelm et al., 2014) during synaptic activity (Sanford et al., 2019). To determine whether the facilitatory effect of Zn^{2+} is mediated by ZnT3, we performed the glutamate uptake assay in preparations from ZnT3 KO mice. Although the KO mice showed no apparent change in the VGLUT1 expression level (Figure S6), the basal glutamate uptake performed in the presence of 1 pM Zn^{2+} was slightly reduced (~20%; Figure 6A), suggesting that ZnT3 is involved in the determination of vesicular glutamate content during resting conditions, concurring with the reduction in the amplitude of excitatory postsynaptic currents observed in the KO (Lavoie et al., 2011). Moreover, the facilitatory effect of Zn^{2+} on glutamate uptake was completely abolished in the KO, implying the existence of an activity-dependent regulation of vesicular glutamate content by Zn^{2+} through ZnT3 (Figure 6B).

Ambient Zn^{2+} increases synaptic quantal size via ZnT3

To test whether the facilitatory effect of Zn^{2+} on vesicular glutamate content leads to an enhanced quantal glutamate release, we measured miniature excitatory postsynaptic currents (mEPSCs) in hippocampal CA3 pyramidal neurons. AMPAR-mediated mEPSC peak amplitude and frequency obtained in the ZnT3 KO mice were decreased when compared with the WT, as reported previously (Figures 7B–7D; Lavoie et al., 2011). Interestingly, the magnitude of reduction in the peak amplitude in the KO (~20%) was comparable to the level of reduction in the glutamate content of ZnT3 KO SVs (see Figure 6A), suggesting that ZnT3 determines the resting synaptic quantal size. The reduction in the frequency was also consistent with the higher calcium sensitivity of SVs observed in the WT (Lavoie et al., 2011). Next, to determine whether Zn^{2+} influences

(G) Distribution of the number of assigned localizations per VGLUT1 cluster.
(H) Distribution of the number of VGLUT1 clusters assigned to each Piccolo site (n = 4 experiments, 59 AZ and 504 VGLUT1 clusters for D–H).
(I) An exemplary two-color composite MINSTED image showing VGLUT1 and ZnT3 localizations (pixel size = 0.3 nm). Each localization is displayed as a Gaussian with a standard deviation given by its estimated localization precision. For better visibility of highly precise localizations, an offset is set at 0.5 nm. The circles represent the two-sigma range around the clusters containing VGLUT1 (purple), ZnT3 (orange), or both localizations (red). The respective confocal Piccolo signal is shown as an overlaid contour plot. The two-sigma range around each cluster's center position is indicated by a circle. Scale bar, 400 nm.
(J and K) Representative VGLUT1 clusters marked in (I) rendered at full precision showing contrasting ZnT3 localization densities. Scale bar, 50 nm.
(L) Summary histogram showing the distribution of the fraction of VGLUT1 localizations per two-color cluster. The pie diagram quantifies the clusters containing VGLUT1 only (purple, 100% VGLUT1 localizations), ZnT3 only (yellow, 100% ZnT3 localizations), and VGLUT1-ZnT3 (red, all intermediate fractions).
(M) Distribution of the lateral distances of the above three SV types to the closest Piccolo site (n = 4 experiments, 59 AZ and 863 clusters for L and M). See also Figure S6.

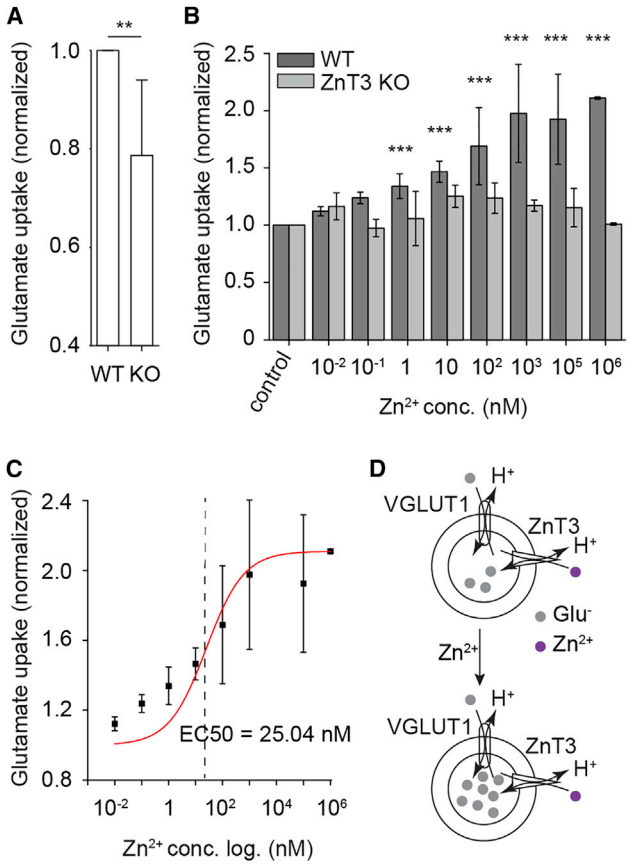

Figure 6. Zn^{2+} facilitates vesicular glutamate content by a mechanism mediated by ZnT3

(A) Bar graph showing enhanced basal vesicular glutamate uptake in SVs (LP2 fraction) isolated from ZnT3 WT mice (WT) in comparison to the KO (*$p < 0.05$, n = 6 experiments, unpaired t test).

(B) Bar graph showing enhancement of glutamate uptake in increasing concentrations of Zn^{2+} in the WT, which is absent in SVs prepared from ZnT3 KO mice. Error bars represent SEM (***$p < 0.001$, n = 6 experiments, two-way ANOVA).

(C) Scatter plot showing dose-dependent facilitation of glutamate uptake by Zn^{2+}. The data points were fitted with a sigmoidal function (Logistic5) to calculate the EC50 value.

(D) Illustration of enhanced vesicular glutamate uptake by Zn^{2+}.

glutamate quantal size, we explored the effect of exogenous application of Zn^{2+}, which increases the cytoplasmic Zn^{2+} concentration (Sanford et al., 2019), on mEPSCs. There was no change in mEPSCs in the presence of 20 μM of Zn^{2+} in the bath solution following a baseline recording (n = 8, data not shown). Since higher concentrations of Zn^{2+} enhanced vesicular glutamate content, we performed the above experiment in the presence of 200 μM of Zn^{2+}. At the higher Zn^{2+} concentration, the mEPSC peak amplitude was significantly increased in the WT (Figures 7B–7D), indicating Zn^{2+}-mediated regulation of glutamatergic quantal size. However, there was no change in the frequency, decay, and rise time kinetics, indicating that ambient Zn^{2+} did not alter release probability or induce postsynaptic changes. No changes in the mEPSC amplitude or frequency (Figures 7B–7D) were detected in the KO, indicating that the increase in glutamate quantal size by the ambient zinc is mediated via ZnT3 and is not due to endocytic uptake of exogenously applied zinc. Overall, the above data demonstrate dose-dependent regulation of synaptic quantal size by Zn^{2+} at glutamatergic synapses via ZnT3 co-present on VGLUT1 SVs.

DISCUSSION

Corelease of multiple neurotransmitters from the same vesicle

Release of multiple neurotransmitters from the same neuron or synapse is well documented (El Mestikawy et al., 2011; Granger et al., 2017; Hnasko and Edwards, 2012). Here, we report quantitative insights on corelease of transmitters from the same vesicle and its impact on synaptic function. We show that (1) nearly 36% of all SVs carry two VTs and are thus capable of storing and releasing distinct neurotransmitters, (2) the SV type containing VGLUT1 and ZnT3 exceedingly accounts for the majority of multi-transporter vesicles (~34% of all SVs), (3) the multi-transporter SVs are more diverse than anticipated, suggesting corelease of all combinations of dual neurotransmitters, and (4) colocalization of VGLUT1 and ZnT3 increases vesicular glutamate content, leading to an enhanced postsynaptic response. We propose that the localization of distinct VTs on the same SVs may signify a specific mechanism to regulate transmitter quantal size and synaptic function.

Since only ~2% of all SVs (excluding those containing VGLUT1) contain more than one VT, we conclude that the majority of neuronal SVs are specific for only one neurotransmitter. However, since this quantification pertains to the whole brain, the relevance of low abundance SVs could be significant if they are enriched in specific brain regions. It is also possible that a small proportion of SVs may carry more than two distinct transporters, as detected at single-cell level (bar plot in Figure S1B), which were not detected in this study. Nonetheless, the unexpected combinatorial diversity of colocalized VTs reveals a new dimension of synaptic fine-tuning that extends well beyond the hitherto documented cases of cotransmission, including some surprising combinations. For example, glutamate-GABA cotransmission has been mostly observed at synapses containing VGLUT2 and VGAT (Root et al., 2014; Shabel et al., 2014). However, our data show that both VGLUT1 and VGLUT2 exhibit similar levels of colocalization with VGAT, reflecting perhaps the lack of extensive studies on VGLUT1-expressing cortical synapses. In addition, only a small fraction of VGAT-positive SVs express another transporter in contrast to the widespread evidence of cotransmission of GABA with other transmitters. This could either reflect the presence of segregated pools of SVs containing GABA and other transmitters at the reported synapses, or that such synapses only make up a small component of the whole inhibitory circuit. It should be noted that mere localization of multiple VTs on individual SVs does not imply corelease because, for some neurotransmitters, this also requires the expression of the synthesizing enzymes. In contrast, it is also known that some VTs are specific for more than one transmitter, such as VGAT (GABA and Glycine) and VMAT2 (all monoamines).

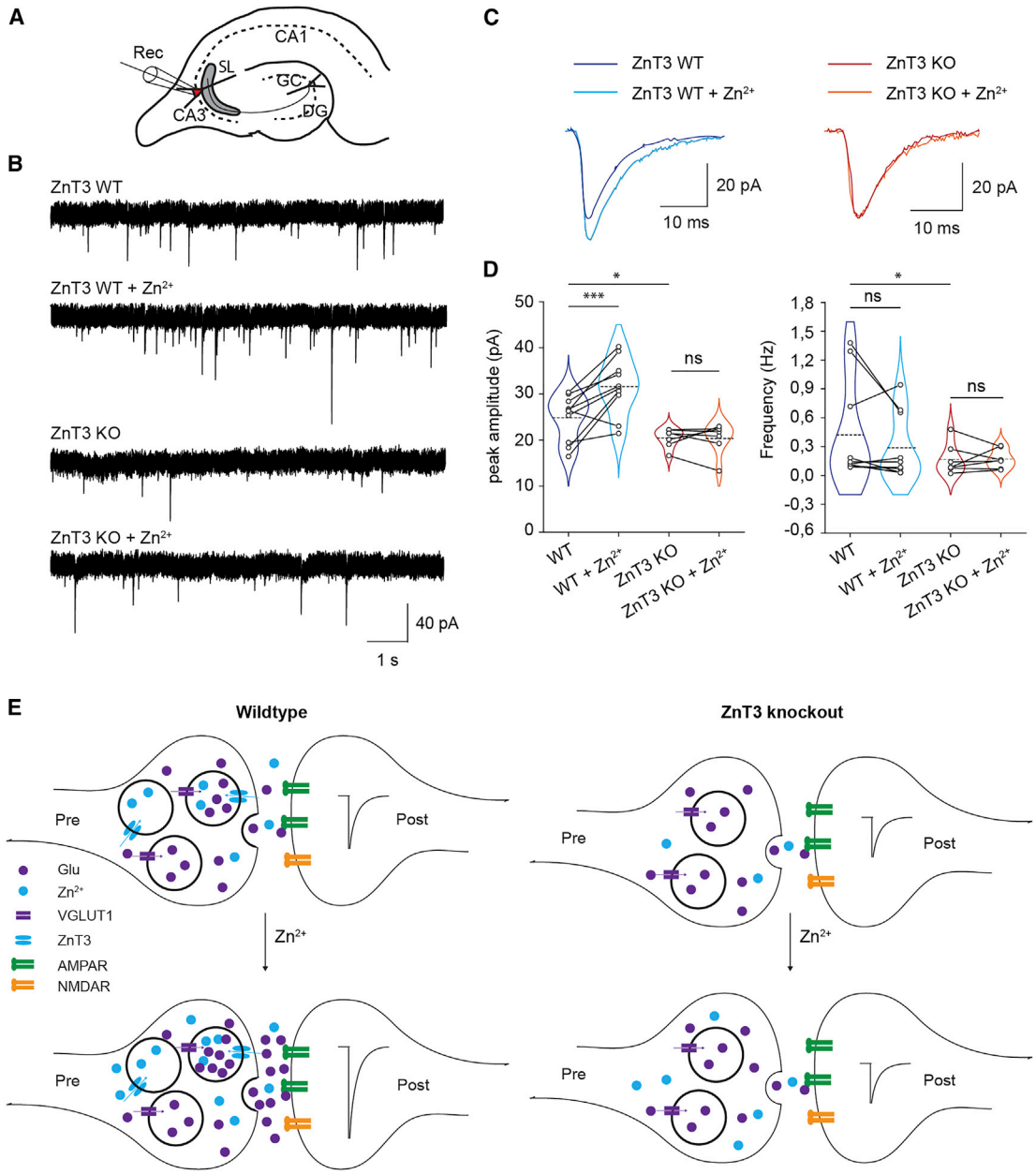

Figure 7. Ambient Zn^{2+} increases synaptic quantal size via ZnT3

(A) Scheme of whole-cell recordings performed on hippocampal CA3 neurons.

(B) Representative traces of mEPSC activity during the baseline recording and after Zn^{2+} application in ZnT3 WT and KO mice.

(C) Average traces showing the time course of mEPSCs during the baseline and after Zn^{2+} application in the WT (left, decay: 6.6 ± 0.4 ms during baseline versus 7.48 ± 0.7 ms after Zn^{2+} application, $p > 0.2$, unpaired t test; rise time: 1.0 ± 0.16 ms during baseline versus 1.1 ± 01 ms after Zn^{2+} application, $p > 0.5$, unpaired t test) and the KO (right, decay: 7.8 ± 1.2 ms during baseline versus 6.8 ± 0.7 ms after Zn^{2+} application, $p > 0.20$, unpaired t test; rise time: 1.15 ± 0.14 ms during baseline versus 1.1 ± 0.1 ms after Zn^{2+} application, $p > 0.5$, unpaired t test).

(D) Violin plots comparing the peak amplitude (left) and frequency (right) of mEPSCs between baseline recordings and after Zn^{2+} application in ZnT3 WT and KO mice. Left: the baseline peak amplitude of mEPSCs was decreased in the KO compared with WT mice (24.9 ± 1.5 pA in WT, n = 10; 20.73 ± 0.7 pA in KO, n = 7; *$p < 0.05$, t test). Following Zn^{2+} application, the peak amplitude significantly increased in the WT (24.9 ± 1.5 pA during baseline; 31.2 ± 1.9 pA after Zn^{2+} application, n = 10, ***$p < 0.002$, unpaired t test) and not in the KO mice (20.7 ± 0.7 pA during baseline; 20.4 ± 1.2 pA after Zn^{2+} application, n = 7, $p > 0.5$, unpaired t test). Right: the baseline frequency was slightly reduced in the KO when compared with the WT (WT, 0.42 ± 0.16 Hz, n = 10; KO, 0.16 ± 0.06 Hz, n = 7, $p < 0.05$, unpaired t test). Following Zn^{2+} application, the frequency did not change in both the WT (0.42 ± 0.1 Hz during baseline; 0.28 ± 0.1 Hz after Zn^{2+} application, $p > 0.1$, unpaired t test, n = 10) and the KO (0.16 ± 0.06 Hz during baseline; 0.17 ± 0.03 Hz after Zn^{2+} application, n = 7, $p > 0.5$, unpaired t test).

(E) Illustration showing the role of ZnT3 in the regulation of glutamate quantal size. Top left: colocalization of VGLUT1 and ZnT3 leads to co-uptake and corelease of glutamate and Zn^{2+} in resting conditions. Bottom left: In the presence of ambient Zn^{2+}, more glutamate is taken up into SVs carrying both VGLUT1 and ZnT3,

(legend continued on next page)

Our study confirms and expands on earlier reports suggesting that the function of expressing different VTs on the same vesicle may not be confined to corelease. For instance, it was shown earlier for neurons expressing VGLUT3 together with either VAChT or VMAT2 that glutamate "synergistically" increases acetylcholine or dopamine accumulation (Gras et al., 2008; Hnasko et al., 2010), but a direct evidence of both transporters being present on the same vesicle was lacking. We report direct colocalization of VGLUT1 and ZnT3 transporters in a large population of SVs and demonstrate that one of the transporters facilitates the activity of the other one, leading to changes in the quantal size of glutamate release. Indeed, ZnT3 SVs containing transporters other than VGLUT1 have also been detected although they are very sparse. As stated earlier, the relevance of these low abundant SVs can only be known by region-specific investigations.

Interestingly, our findings lend further support to the notion of vesicle heterogeneity at individual synapses despite VGLUT1 and ZnT3 following similar trafficking routes (Salazar et al., 2005). In dopaminergic neurons, glutamate and dopamine release from the same terminals is differentially regulated, suggesting differential sorting of these VTs into different SV subsets (Silm et al., 2019). However, it remains to be explored whether VGLUT1 SVs containing ZnT3 are differentially regulated from those lacking it in the same synapses, particularly in the light of differences in the AZ structure between dopaminergic and glutamatergic synapses (Banerjee et al., 2022). Furthermore, the new data provide ultrastructural evidence for earlier findings of the temporally coinciding release of Zn^{2+} and glutamate at specific synapses (Lavoie et al., 2011; Vergnano et al., 2014).

Single-vesicle investigations from whole brain preparations do exist (Chantranupong et al., 2020; Farsi et al., 2016; Mutch et al., 2011). For example, Mutch and colleagues profiled copy numbers of specific SV proteins using single-vesicle imaging to assess the precision of protein sorting to vesicles. They showed little intervesicular variation in the copy numbers for SV2, VATPase, VGLUT1, and synaptotagmin 1 when compared with Syb2, Syp, and Synaptogyrin, indicating differential protein sorting fidelity between SV proteins (Mutch et al., 2011). However, this study reveals a highly variable copy number for VGLUT1, suggesting the requirement for a direct evaluation of copy numbers of SV proteins in specific and intact synapses.

Synaptic and circuit function implications of the high overlap between VGLUT1 and ZnT3

Corelease of neurotransmitters from the same SV pools has been demonstrated in some synapses, but the effect on synaptic computation and circuit function has been addressed only in a few studies (Liu et al., 2013; Shabel et al., 2014). Since the functional implications of corelease of distinct transmitters depend on various factors, including the identity of neurotransmitters, the localization of pre- and postsynaptic receptors, and activity-dependent changes of the constituents (if any), a generalized scheme of synaptic signaling is difficult to achieve. However, a common feature can be hypothesized for SVs that are specific for VGLUT1-ZnT3 SVs. For example, the effect of glutamate and Zn^{2+} on the postsynaptic AMPA and NMDA receptors is well established. While glutamate elicits an excitatory response, Zn^{2+} inhibits the same (Kalappa et al., 2015; Vergnano et al., 2014). Thus, the corelease of these two fast antagonistic neurotransmitters might primarily act to strongly finetune the excitation window, as observed in glutamate-GABA coreleasing neurons (Shabel et al., 2014). When compared with the inhibitory circuit, mediated by GABA that predominantly balances excitation through a separate population of inhibitory neurons, Zn^{2+} is spatiotemporally locked with glutamate release to modulate excitation. Thus, considering the vast abundance of VGLUT1-ZnT3 SVs, Zn^{2+} action could underlie a systemic and robust mechanism to modulate excitation. It will also be interesting to test whether the facilitation of glutamate release by Zn^{2+} is part of a synaptic adaptation mechanism to compensate for NMDAR blockade and the resulting reduced postsynaptic calcium influx by synaptically released zinc.

Indeed, synaptic zinc, released by short trains of stimuli, selectively inhibits postsynaptic GluN2A-NMDARs and causes changes in synaptic integration and plasticity (Vergnano et al., 2014). It is, however, highly conceivable that such a direct effect depends on the magnitude of synaptic Zn^{2+} at a particular synapse, which relies on the expression level/copy number of ZnT3 in individual SVs. As the copy number of ZnT3 is highly heterogeneous (between 1 and 8, as determined in the present study), a region-specific zinc action depending on the expression level of ZnT3 is more plausible.

Unlike other neurotransmitters, Zn^{2+} is not synthesized by an enzymatic machinery; instead, its cytoplasmic concentration is regulated by neuronal activity (Minckley et al., 2019; Sanford et al., 2019), which could lead to activity-dependent regulation of quantal glutamate mediated by ZnT3. To our knowledge, this is the first evidence of a direct role of zinc, which has been implicated in several neurodegenerative conditions and synaptic pathologies (Frederickson et al., 2005; Kawahara et al., 2020; Trist et al., 2018), in the molecular mechanisms leading to changes in synaptic strength.

STAR★METHODS

Detailed methods are provided in the online version of this paper and include the following:

- KEY RESOURCES TABLE
- RESOURCE AVAILABILITY
  - Lead contact
  - Materials availability
  - Data and code availability
- EXPERIMENTAL MODEL AND SUBJECT DETAILS
  - Animals

leading to enhanced glutamate release and postsynaptic response. Top right: genetic deletion of ZnT3 leads to reduced vesicular glutamate content and postsynaptic response at resting conditions. Bottom right: absence of ZnT3 does not affect vesicular glutamate content or postsynaptic response in the presence of ambient Zn^{2+}. The data demonstrate that colocalization of ZnT3 and VGLUT1 is critical for Zn^{2+} mediated regulation of glutamatergic neurotransmission and suggest coupling of activity of the two transporters.

SUPPLEMENTAL INFORMATION

Supplemental information can be found online at https://doi.org/10.1016/j.neuron.2022.02.008.

ACKNOWLEDGMENTS

We thank members of the R.J. lab for useful discussions, Raza-Ur Rahman (Broad Institute) for RSeq analysis, Brigitte Barg-Kues for genotyping, and Sigrid Schmidt for preparing culture neurons. We thank Gudrun Ahnert-Hilger (Berlin), Silvio Rizzoli (Göttingen), Pablo Castillo (New York), and Agata Witkowska (Berlin) for helpful comments on the manuscript. This research project was conducted with support from the Volkswagen Foundation ("Experiment" grant to S.S.), the European Research Council Advanced Grant (SVNeuroTrans to R.J.), the John Black Charitable Foundation (to I.M.), and Deutsche Forschungsgemeinschaft (SFB1286 to H.U.). H.v.d.E. is part of the Max Planck School of Photonics supported by BMBF, Max Planck Society, and Fraunhofer Society. J.P. was funded by the Deutsche Forschungsgemeinschaft (DFG, German Research Foundation) under Germany's Excellence Strategy—EXC 2067/1-390729940.

AUTHOR CONTRIBUTIONS

S.S. conceptualized the study, performed and supervised experiments, evaluated all data, and wrote the paper with inputs from all co-authors. R.J. provided input and appraised all data. S.W.H. provided input on STED and MINSTED experiments. N.U., V.N.M., J.P., M.G., L.B., and E.Z. designed and performed different aspects of the study. H.v.d.E. performed and analyzed MINSTED experiments, and M.L. contributed to the cluster analysis. J.J. and I.M. performed and analyzed electrophysiology experiments. M.N., I.S., and H.U. performed mass spectrometry studies and analyzed data. A.Z.P. drafted and wrote the imaging analysis workflow. D.R. performed electron microscopy and analyzed data.

DECLARATION OF INTERESTS

The authors declare no competing interests.

INCLUSION AND DIVERSITY

One or more of the authors of this paper self-identifies as a member of the LGBTQ+ community.

Received: July 27, 2021
Revised: January 8, 2022
Accepted: February 10, 2022
Published: March 8, 2022

REFERENCES

Banerjee, A., Imig, C., Balakrishnan, K., Kershberg, L., Lipstein, N., Uronen, R.L., Wang, J., Cai, X., Benseler, F., Rhee, J.S., et al. (2022). Molecular and functional architecture of striatal dopamine release sites. Neuron *110*, 248.e9–265.e9.

Birinci, Y., Preobraschenski, J., Ganzella, M., Jahn, R., and Park, Y. (2020). Isolation of large dense-core vesicles from bovine adrenal medulla for functional studies. Sci. Rep. *10*, 7540.

Bruderer, R., Bernhardt, O.M., Gandhi, T., Miladinović, S.M., Cheng, L.Y., Messner, S., Ehrenberger, T., Zanotelli, V., Butscheid, Y., Escher, C., et al. (2015). Extending the limits of quantitative proteome profiling with data-independent acquisition and application to acetaminophen-treated three-dimensional liver microtissues. Mol. Cell. Proteomics *14*, 1400–1410.

Chantranupong, L., Saulnier, J.L., Wang, W., Jones, D.R., Pacold, M.E., and Sabatini, B.L. (2020). Rapid purification and metabolomic profiling of synaptic vesicles from mammalian brain. eLife *9*, e59699.

Chuhma, N., Mingote, S., Moore, H., and Rayport, S. (2014). Dopamine neurons control striatal cholinergic neurons via regionally heterogeneous dopamine and glutamate signaling. Neuron *81*, 901–912.

Clements, J.D., and Bekkers, J.M. (1997). Detection of spontaneous synaptic events with an optimally scaled template. Biophys. J. *73*, 220–229.

Cole, T.B., Wenzel, H.J., Kafer, K.E., Schwartzkroin, P.A., and Palmiter, R.D. (1999). Elimination of zinc from synaptic vesicles in the intact mouse brain by disruption of the ZnT3 gene. Proc. Natl. Acad. Sci. USA *96*, 1716–1721.

El Mestikawy, S., Wallén-Mackenzie, A., Fortin, G.M., Descarries, L., and Trudeau, L.E. (2011). From glutamate co-release to vesicular synergy: vesicular glutamate transporters. Nat. Rev. Neurosci. *12*, 204–216.

Farsi, Z., Preobraschenski, J., van den Bogaart, G., Riedel, D., Jahn, R., and Woehler, A. (2016). Single-vesicle imaging reveals different transport mechanisms between glutamatergic and GABAergic vesicles. Science *351*, 981–984.

Fasano, C., Rocchetti, J., Pietrajtis, K., Zander, J.F., Manseau, F., Sakae, D.Y., Marcus-Sells, M., Ramet, L., Morel, L.J., Carrel, D., et al. (2017). Regulation of the hippocampal network by VGLUT3-positive CCK- GABAergic basket cells. Front. Cell. Neurosci. *11*, 140.

Frahm, S., Antolin-Fontes, B., Görlich, A., Zander, J.F., Ahnert-Hilger, G., and Ibañez-Tallon, I. (2015). An essential role of acetylcholine-glutamate synergy at habenular synapses in nicotine dependence. eLife *4*, e11396.

Frederickson, C.J., Koh, J.Y., and Bush, A.I. (2005). The neurobiology of zinc in health and disease. Nat. Rev. Neurosci. *6*, 449–462.

Geumann, U., Barysch, S.V., Hoopmann, P., Jahn, R., and Rizzoli, S.O. (2008). SNARE function is not involved in early endosome docking. Mol. Biol. Cell *19*, 5327–5337.

Goch, W., and Bal, W. (2020). Stochastic or not? Method to predict and quantify the stochastic effects on the association reaction equilibria in nanoscopic systems. J. Phys. Chem. A *124*, 1421–1428.

Göttfert, F., Pleiner, T., Heine, J., Westphal, V., Görlich, D., Sahl, S.J., and Hell, S.W. (2017). Strong signal increase in STED fluorescence microscopy by imaging regions of subdiffraction extent. Proc. Natl. Acad. Sci. USA *114*, 2125–2130.

Granger, A.J., Wallace, M.L., and Sabatini, B.L. (2017). Multi-transmitter neurons in the mammalian central nervous system. Curr. Opin. Neurobiol. *45*, 85–91.

Gras, C., Amilhon, B., Lepicard, E.M., Poirel, O., Vinatier, J., Herbin, M., Dumas, S., Tzavara, E.T., Wade, M.R., Nomikos, G.G., et al. (2008). The vesicular glutamate transporter VGLUT3 synergizes striatal acetylcholine tone. Nat. Neurosci. *11*, 292–300.

Grønborg, M., Pavlos, N.J., Brunk, I., Chua, J.J., Münster-Wandowski, A., Riedel, D., Ahnert-Hilger, G., Urlaub, H., and Jahn, R. (2010). Quantitative comparison of glutamatergic and GABAergic synaptic vesicles unveils selectivity for few proteins including MAL2, a novel synaptic vesicle protein. J. Neurosci. *30*, 2–12.

Heine, J., Reuss, M., Harke, B., D'Este, E., Sahl, S.J., and Hell, S.W. (2017). Adaptive-illumination STED nanoscopy. Proc. Natl. Acad. Sci. USA *114*, 9797–9802.

Herzog, E., Takamori, S., Jahn, R., Brose, N., and Wojcik, S.M. (2006). Synaptic and vesicular co-localization of the glutamate transporters VGLUT1 and VGLUT2 in the mouse hippocampus. J. Neurochem. *99*, 1011–1018.

Higley, M.J., Gittis, A.H., Oldenburg, I.A., Balthasar, N., Seal, R.P., Edwards, R.H., Lowell, B.B., Kreitzer, A.C., and Sabatini, B.L. (2011). Cholinergic interneurons mediate fast VGluT3-dependent glutamatergic transmission in the striatum. PLoS One *6*, e19155.

Hnasko, T.S., Chuhma, N., Zhang, H., Goh, G.Y., Sulzer, D., Palmiter, R.D., Rayport, S., and Edwards, R.H. (2010). Vesicular glutamate transport promotes dopamine storage and glutamate corelease in vivo. Neuron *65*, 643–656.

Hnasko, T.S., and Edwards, R.H. (2012). Neurotransmitter corelease: mechanism and physiological role. Annu. Rev. Physiol. *74*, 225–243.

Hughes, C.S., Moggridge, S., Müller, T., Sorensen, P.H., Morin, G.B., and Krijgsveld, J. (2019). Single-pot, solid-phase-enhanced sample preparation for proteomics experiments. Nat. Protoc. *14*, 68–85.

Huttner, W.B., Schiebler, W., Greengard, P., and De Camilli, P. (1983). Synapsin I (protein I), a nerve terminal-specific phosphoprotein. III. Its association with synaptic vesicles studied in a highly purified synaptic vesicle preparation. J. Cell Biol. *96*, 1374–1388.

Jahn, R., Schiebler, W., Ouimet, C., and Greengard, P. (1985). A 38,000-dalton membrane protein (p38) present in synaptic vesicles. Proc. Natl. Acad. Sci. USA *82*, 4137–4141.

Kaech, S., and Banker, G. (2006). Culturing hippocampal neurons. Nat. Protoc. *1*, 2406–2415.

Kalappa, B.I., Anderson, C.T., Goldberg, J.M., Lippard, S.J., and Tzounopoulos, T. (2015). AMPA receptor inhibition by synaptically released zinc. Proc. Natl. Acad. Sci. USA *112*, 15749–15754.

Kawahara, M., Kato-Negishi, M., and Tanaka, K.I. (2020). Amyloids: regulators of metal homeostasis in the synapse. Molecules *25*, 1441.

Lavoie, N., Jeyaraju, D.V., Peralta, M.R., 3rd, Seress, L., Pellegrini, L., and Tóth, K. (2011). Vesicular zinc regulates the Ca2+ sensitivity of a subpopulation of presynaptic vesicles at hippocampal mossy fiber terminals. J. Neurosci. *31*, 18251–18265.

Levet, F., Hosy, E., Kechkar, A., Butler, C., Beghin, A., Choquet, D., and Sibarita, J.B. (2015). SR-Tesseler: a method to segment and quantify localization-based super-resolution microscopy data. Nat. Methods *12*, 1065–1071.

Liu, S., Plachez, C., Shao, Z., Puche, A., and Shipley, M.T. (2013). Olfactory bulb short axon cell release of GABA and dopamine produces a temporally biphasic inhibition-excitation response in external tufted cells. J. Neurosci. *33*, 2916–2926.

Malkusch, S., Endesfelder, U., Mondry, J., Gelléri, M., Verveer, P.J., and Heilemann, M. (2012). Coordinate-based colocalization analysis of single-molecule localization microscopy data. Histochem. Cell Biol. *137*, 1–10.

Marvin, J.S., Borghuis, B.G., Tian, L., Cichon, J., Harnett, M.T., Akerboom, J., Gordus, A., Renninger, S.L., Chen, T.W., Bargmann, C.I., et al. (2013). An optimized fluorescent probe for visualizing glutamate neurotransmission. Nat. Methods *10*, 162–170.

Marvin, J.S., Scholl, B., Wilson, D.E., Podgorski, K., Kazemipour, A., Müller, J.A., Schoch, S., Quiroz, F.J.U., Rebola, N., Bao, H., et al. (2018). Stability, affinity, and chromatic variants of the glutamate sensor iGluSnFR. Nat. Methods *15*, 936–939.

McAllister, B.B., and Dyck, R.H. (2017). Zinc transporter 3 (ZnT3) and vesicular zinc in central nervous system function. Neurosci. Biobehav. Rev. *80*, 329–350.

Minckley, T.F., Zhang, C., Fudge, D.H., Dischler, A.M., LeJeune, K.D., Xu, H., and Qin, Y. (2019). Sub-nanomolar sensitive GZnP3 reveals TRPML1-mediated neuronal Zn^{2+} signals. Nat. Commun. *10*, 4806.

Mutch, S.A., Kensel-Hammes, P., Gadd, J.C., Fujimoto, B.S., Allen, R.W., Schiro, P.G., Lorenz, R.M., Kuyper, C.L., Kuo, J.S., Bajjalieh, S.M., et al. (2011). Protein quantification at the single vesicle level reveals that a subset of synaptic vesicle proteins are trafficked with high precision. J. Neurosci. *31*, 1461–1470.

Ovesný, M., Křížek, P., Borkovec, J., Svindrych, Z., and Hagen, G.M. (2014). ThunderSTORM: a comprehensive ImageJ plug-in for PALM and STORM data analysis and super-resolution imaging. Bioinformatics *30*, 2389–2390.

Perez-Riverol, Y., Csordas, A., Bai, J., Bernal-Llinares, M., Hewapathirana, S., Kundu, D.J., Inuganti, A., Griss, J., Mayer, G., Eisenacher, M., et al. (2019). The PRIDE database and related tools and resources in 2019: improving support for quantification data. Nucleic Acids Res. *47*, D442–D450.

Preobraschenski, J., Zander, J.F., Suzuki, T., Ahnert-Hilger, G., and Jahn, R. (2014). Vesicular glutamate transporters use flexible anion and cation binding sites for efficient accumulation of neurotransmitter. Neuron *84*, 1287–1301.

Qin, Y., Dittmer, P.J., Park, J.G., Jansen, K.B., and Palmer, A.E. (2011). Measuring steady-state and dynamic endoplasmic reticulum and Golgi Zn2+ with genetically encoded sensors. Proc. Natl. Acad. Sci. USA *108*, 7351–7356.

Ren, J., Qin, C., Hu, F., Tan, J., Qiu, L., Zhao, S., Feng, G., and Luo, M. (2011). Habenula "cholinergic" neurons co-release glutamate and acetylcholine and activate postsynaptic neurons via distinct transmission modes. Neuron *69*, 445–452.

Root, D.H., Mejias-Aponte, C.A., Zhang, S., Wang, H.L., Hoffman, A.F., Lupica, C.R., and Morales, M. (2014). Single rodent mesohabenular axons release glutamate and GABA. Nat. Neurosci. *17*, 1543–1551.

Root, D.H., Zhang, S., Barker, D.J., Miranda-Barrientos, J., Liu, B., Wang, H.L., and Morales, M. (2018). Selective brain distribution and distinctive synaptic architecture of dual glutamatergic-GABAergic neurons. Cell Rep. *23*, 3465–3479.

Salazar, G., Craige, B., Love, R., Kalman, D., and Faundez, V. (2005). Vglut1 and ZnT3 co-targeting mechanisms regulate vesicular zinc stores in PC12 cells. J. Cell Sci. *118*, 1911–1921.

Sanford, L., Carpenter, M.C., and Palmer, A.E. (2019). Intracellular Zn^{2+} transients modulate global gene expression in dissociated rat hippocampal neurons. Sci. Rep. *9*, 9411.

Saunders, A., Granger, A.J., and Sabatini, B.L. (2015). Corelease of acetylcholine and GABA from cholinergic forebrain neurons. eLife *4*, e06412.

Schägger, H. (2006). Tricine-SDS-PAGE. Nat. Protoc. *1*, 16–22.

Schneider, C.A., Rasband, W.S., and Eliceiri, K.W. (2012). NIH Image to ImageJ: 25 years of image analysis. Nat. Methods *9*, 671–675.

Schnitzbauer, J., Strauss, M.T., Schlichthaerle, T., Schueder, F., and Jungmann, R. (2017). Super-resolution microscopy with DNA-PAINT. Nat. Protoc. *12*, 1198–1228.

Schwanhäusser, B., Busse, D., Li, N., Dittmar, G., Schuchhardt, J., Wolf, J., Chen, W., and Selbach, M. (2011). Global quantification of mammalian gene expression control. Nature *473*, 337–342.

SenGupta, A., Bocchio, M., Bannerman, D.M., Sharp, T., and Capogna, M. (2017). Control of amygdala circuits by 5-HT neurons via 5-HT and glutamate Cotransmission. J. Neurosci. *37*, 1785–1796.

Shabel, S.J., Proulx, C.D., Piriz, J., and Malinow, R. (2014). Mood regulation. GABA/glutamate co-release controls habenula output and is modified by antidepressant treatment. Science *345*, 1494–1498.

Shaw, A., Hoffecker, I.T., Smyrlaki, I., Rosa, J., Grevys, A., Bratlie, D., Sandlie, I., Michaelsen, T.E., Andersen, J.T., and Högberg, B. (2019). Binding to nanopatterned antigens is dominated by the spatial tolerance of antibodies. Nat. Nanotechnol. *14*, 184–190.

Silm, K., Yang, J., Marcott, P.F., Asensio, C.S., Eriksen, J., Guthrie, D.A., Newman, A.H., Ford, C.P., and Edwards, R.H. (2019). Synaptic vesicle recycling pathway determines neurotransmitter content and release properties. Neuron *102*, 786.e5–800.e5.

Sograte-Idrissi, S., Schlichthaerle, T., Duque-Afonso, C.J., Alevra, M., Strauss, S., Moser, T., Jungmann, R., Rizzoli, S.O., and Opazo, F. (2020). Circumvention of common labelling artefacts using secondary nanobodies. Nanoscale *12*, 10226–10239.

Stuber, G.D., Hnasko, T.S., Britt, J.P., Edwards, R.H., and Bonci, A. (2010). Dopaminergic terminals in the nucleus accumbens but not the dorsal striatum corelease glutamate. J Neurosci *30*, 8229–8233.

Takács, V.T., Cserép, C., Schlingloff, D., Pósfai, B., Szőnyi, A., Sos, K.E., Környei, Z., Dénes, Á., Gulyás, A.I., Freund, T.F., and Nyiri, G. (2018). Co-transmission of acetylcholine and GABA regulates hippocampal states. Nat. Commun. *9*, 2848.

Takamori, S., Holt, M., Stenius, K., Lemke, E.A., Grønborg, M., Riedel, D., Urlaub, H., Schenck, S., Brügger, B., Ringler, P., et al. (2006). Molecular anatomy of a trafficking organelle. Cell *127*, 831–846.

Takamori, S., Rhee, J.S., Rosenmund, C., and Jahn, R. (2001). Identification of differentiation-associated brain-specific phosphate transporter as a second vesicular glutamate transporter (VGLUT2). J. Neurosci. *21*, RC182.

Takamori, S., Riedel, D., and Jahn, R. (2000). Immunoisolation of GABA-specific synaptic vesicles defines a functionally distinct subset of synaptic vesicles. J. Neurosci. *20*, 4904–4911.

Taoufiq, Z., Ninov, M., Villar-Briones, A., Wang, H.Y., Sasaki, T., Roy, M.C., Beauchain, F., Mori, Y., Yoshida, T., Takamori, S., et al. (2020). Hidden proteome of synaptic vesicles in the mammalian brain. Proc. Natl. Acad. Sci. USA *117*, 33586–33596.

Trist, B.G., Hare, D.J., and Double, K.L. (2018). A proposed mechanism for neurodegeneration in movement disorders characterized by metal dyshomeostasis and oxidative stress. Cell Chem. Biol. *25*, 807–816.

Tritsch, N.X., Ding, J.B., and Sabatini, B.L. (2012). Dopaminergic neurons inhibit striatal output through non-canonical release of GABA. Nature *490*, 262–266.

Tritsch, N.X., Granger, A.J., and Sabatini, B.L. (2016). Mechanisms and functions of GABA co-release. Nat. Rev. Neurosci. *17*, 139–145.

Trudeau, L.E., and El Mestikawy, S. (2018). Glutamate cotransmission in cholinergic, GABAergic and monoamine systems: contrasts and commonalities. Front. Neural Circuits *12*, 113.

Consortium, UniProt (2019). UniProt: a worldwide hub of protein knowledge. Nucleic Acids Res. *47*, D506–D515.

Vaaga, C.E., Borisovska, M., and Westbrook, G.L. (2014). Dual-transmitter neurons: functional implications of co-release and co-transmission. Curr. Opin. Neurobiol. *29*, 25–32.

Varga, V., Losonczy, A., Zemelman, B.V., Borhegyi, Z., Nyiri, G., Domonkos, A., Hangya, B., Holderith, N., Magee, J.C., and Freund, T.F. (2009). Fast synaptic subcortical control of hippocampal circuits. Science *326*, 449–453.

Vergnano, A.M., Rebola, N., Savtchenko, L.P., Pinheiro, P.S., Casado, M., Kieffer, B.L., Rusakov, D.A., Mulle, C., and Paoletti, P. (2014). Zinc dynamics and action at excitatory synapses. Neuron *82*, 1101–1114.

Vinkenborg, J.L., Nicolson, T.J., Bellomo, E.A., Koay, M.S., Rutter, G.A., and Merkx, M. (2009). Genetically encoded FRET sensors to monitor intracellular Zn2+ homeostasis. Nat. Methods *6*, 737–740.

Weber, M., Leutenegger, M., Stoldt, S., Jakobs, S., Mihaila, T.S., Butkevich, A.N., and Hell, S.W. (2021). MINSTED fluorescence localization and nanoscopy. Nat. Photonics *15*, 361–366.

Wilhelm, B.G., Mandad, S., Truckenbrodt, S., Kröhnert, K., Schäfer, C., Rammner, B., Koo, S.J., Claßen, G.A., Krauss, M., Haucke, V., et al. (2014). Composition of isolated synaptic boutons reveals the amounts of vesicle trafficking proteins. Science *344*, 1023–1028.

Zander, J.F., Münster-Wandowski, A., Brunk, I., Pahner, I., Gómez-Lira, G., Heinemann, U., Gutiérrez, R., Laube, G., and Ahnert-Hilger, G. (2010). Synaptic and vesicular coexistence of VGLUT and VGAT in selected excitatory and inhibitory synapses. J. Neurosci. *30*, 7634–7645.

Zeisel, A., Hochgerner, H., Lönnerberg, P., Johnsson, A., Memic, F., van der Zwan, J., Häring, M., Braun, E., Borm, L.E., La Manno, G., et al. (2018). Molecular architecture of the mouse nervous system. Cell *174*, 999.e22–1014.e22.

Zimmermann, J., Herman, M.A., and Rosenmund, C. (2015). Co-release of glutamate and GABA from single vesicles in GABAergic neurons exogenously expressing VGLUT3. Front. Synaptic Neurosci. *7*, 16.

STAR★METHODS

KEY RESOURCES TABLE

REAGENT or RESOURCE	SOURCE	IDENTIFIER
Antibodies		
VGLUT 1	Synaptic System	Cat# 135011; RRID: AB_2884913
VGLUT 1	Synaptic System	Cat# 135303; RRID: AB_887875
VGLUT 2	Synaptic System	Cat# 135421; RRID: AB_2884916
VGLUT 2	Synaptic System	Cat# 135211; RRID: AB_887883
VGLUT 3	Synaptic System	Cat# 135203; RRID: AB_2636917
VGLUT 3	Synaptic System	Cat# 131011; RRID: AB_887886
VGAT	Synaptic System	Cat# 139103; RRID: AB_2619818
VAChT	Synaptic System	Cat# 138313; RRID: AB_887864
VMAT2	Synaptic System	Cat# 197011; RRID: AB_2619826
ZnT3	Synaptic System	Cat# 119003; RRID: AB_2619888
SV2A	Synaptic System	Cat# 119102; RRID: AB_2725760
SV2B	Synaptic System	Cat# 119102; RRID: AB_887803
Syntaxin 1	Synaptic System	Cat# 110011; RRID: AB_887842
IRDye 800CW anti-mouse IgG	LI-COR	Cat# 926-32212; RRID: AB_621847
IRDye 800CW anti-rabbit IgG	LI-COR	Cat# 926-32213; RRID: AB_621848
IRDye 680RD anti-guinea pig IgG	LI-COR	Cat# 926-68077; RRID: AB_10956079
Synaptophysin	Synaptic System	Cat# 101002; RRID: AB_887905
Synaptobrevin2	Synaptic System	Cat# 104 211BT; RRID: AB_2619758
Piccolo	Synaptic System	Cat# 142104; RRID: AB_2619831
Goat anti-rabbit IgG-Alexa Fluor ™ 594	Invitrogen	Cat# A11012; RRID: AB_2534079
Goat anti-Guinea pig IgG- Alexa Fluor ™ 488	Thermofisher Scientific	Cat# A11073; RRID: AB_2534117
Goat anti-mouse IgG-Abberior STAR RED	Abberior	Cat# STRED-1001; RRID: AB_2847853
FluoTag®-X2 anti-Mouse Immunoglobulin kappa light chain	NanoTag Technologies	Cat# N1202
Bacterial and virus strains		
Biological samples	N/A	N/A
Chemicals, peptides, and recombinant proteins		
ProLong™ Diamond Antifade Mountant	Thermofisher Scientific	Cat# P36961
FCCP	Focus Biomolecules	Cat# 10-1182
Pierce™ BCA Protein Assay Kit	Thermofisher Scientific	Cat# 23225
HEPES	Sigma Aldrich	Cat# H3375
TCEP	Thermo Scientific	Cat# 77720
Chloroacetamide	Sigma Aldrich	Cat# 22790
Proteomics Dynamic Range Standard Set	Sigma-Aldrich	Cat# UPS2-1SET
Magnetic beads with carboxylate modified surface	GE Healthcare	Cat# GE45152105050250
LysC-protease	Promega	Cat# VA1170
Trypsin	Promega	Cat# V5111
Acetonitrile (ACN)	Sigma Aldrich	Cat# 1.00030.2500
Trifluoroacetic acid (TFA)	ROTH	Cat# P088.1
Formic Acid	Fluka	Cat# 56302-50ML-F

(*Continued on next page*)

Continued

REAGENT or RESOURCE	SOURCE	IDENTIFIER
Deposited data		
Mass spectrometry raw data	This paper	www.proteomexchange.org; PXD025318
Experimental models: Organisms/strains		
Wistar rats	Charles River	RRID: RGD_734476
Mouse: C57BL/6N	The Jackson Laboratory	JAX: 005304; RRID: IMSR_JAX:005304
ZnT3 knockout (C57BL/6N)	Cole et al., 1999	MGI Cat# 3029270; RRID: MGI:3029270
Software and algorithms		
Illustrator CS6	Adobe	https://www.adobe.com/
OriginPro 2020	OriginLab Corporation	https://www.originlab.com/
RStudio v1.2.5033	Rstudio	https://www.rstudio.com/
FIJI	Schneider et al., 2012	https://imagej.nih.gov/ij/
Igor Pro 6.36	Wavemetrics	https://www.wavemetrics.com/products/igorpro
BioRender	BioRender.com	https://biorender.com/

RESOURCE AVAILABILITY

Lead contact

Further information and requests for resources and reagents should be directed to and will be fulfilled by the lead contact, Sivakumar Sambandan (siva.sambandan@mpinat.mpg.de).

Materials availability

Reagents used in the study were of general use and from commercial sources.

Data and code availability

- Mass spectrometry raw data and analyses files have been deposited at www.proteomexchange.org and are publicly available as of the date of publication. Accession numbers are listed in the key resources table.
- This paper does not report original code.
- Any additional information required to reanalyze the data reported in this paper is available from the lead contact upon request.

EXPERIMENTAL MODEL AND SUBJECT DETAILS

Animals

Wistar rats and ZnT3 WT and KO mice (C57BL/6 mice, RRID:MGI:3029270) were used in the study. All experimental procedures involving the use of rats and mice were carried out in accordance with national and institutional guidelines. All animals in the study, including wild type and transgenic mice, were bred at the Max Planck Institute. Both, mouse and rat SVs were prepared from ~6 weeks old animals of both sexes. Hippocampal primary culture neurons were prepared from wistar rats.

METHOD DETAILS

Vesicle preparation

Isolation of synaptic vesicles from rat brain was performed as described before (Huttner et al., 1983; Takamori et al., 2006). Typically, twenty animals were used per preparation which includes multiple fractionation steps and a final control-pore glass bead chromatography (CPG) column purification step. CPG-SVs were taken from fractions containing the highest concentration of SVs for further studies. All fluorescent imaging experiments and quantitative immunoblotting were performed using freshly prepared SVs, avoiding pelleting or freezing that causes aggregation.

LP2 fraction of mice SVs were prepared following a similar protocol as that of rats except that the volume of the buffers were scaled down to half because of the small size of mouse brains. Typically, 10 wildtype (WT) mice and 10 knockout (KO) mice were sacrificed together and the SV isolation for WT and KO was performed simultaneously.

Chromaffin granules were isolated from bovine adrenal medulla by combining differential and discontinuous (0.3 M/1.8 M) sucrose gradient centrifugation (Birinci et al., 2020).

Dynamic Light Scattering

Dynamic light scattering (DLS) was used to determine the size distribution and integrity of synaptic vesicles following purification. Measurements were carried out with 25 μl of SV sample, using a DynaPro™ Dynamic Light Scattering Instrument (Wyatt Technology) at a laser power of 5 % with 20 s acquisition duration. Individual measurements were performed 10 times and the values were averaged.

Electron microscopy

To evaluate the purity and quality of prepared synaptic vesicles, negative staining was regularly performed. The sample was bound to carbon coated, glow discharged grids and counterstained using 1% uranyl acetate. For immunogold-labeling (IEM, Figure S4), purified SVs were absorbed to formvar coated grids, fixed with 4% paraformaldehyde, quenched with 20 mM glycine and immunostained using the described antibody, followed by addition of Protein A-gold (10 nm). The grids were then rinsed repeatedly with TPBS and high-salt TPBS (0.5 M NaCl) and post-fixed with 2% glutaraldehyde. For double labeling (Figure 3), the first immunoreaction was blocked by fixation with 1% glutaraldehyde, followed by a second immunogold labeling. After counterstained with 1% uranyl acetate, samples were investigated using Talos L120C (Thermo Fisher Scientifc). The antibodies were used in reverse order as well to exclude the effects of glutaraldehyde fixation on the antigenicity. Antibodies used in IEM are published previously (Syp, clone G95, rabbit polyclonal, (Jahn et al., 1985)) and Synaptic Systems, Germany (Syb2-104211; VGLUT1-135303; ZnT3-197011.

SV immunolabeling for DyMIN STED Imaging

Purified SVs were resuspended in blocking solution [PBS, pH 7.4, 5% normal goat serum (v/v)] with constant rotation for 1 h at room temperature (RT). Primary antibodies or fluorophore conjugated primary antibodies were added in blocking solution containing SVs at a concentration of 6μg/ml. with constant rotation for 1 h at RT. Subsequently, the SV sample was subjected to size exclusion chromatography (SEC) using a superdex 200 column by means of ÄKTA system (GE Healthcare) to purify labeled SVs from unbound antibodies. As expected, the SVs were eluted in void volume and the antibodies and excess serum proteins were eluted via the stationary phase, resulting in clear separate peaks for SVs and smaller contaminants (Figure S2). The SVs were typically eluted at ~14ml elution volume corresponding to elution fractions 36 to 37.

Following SEC purification, SV integrity was again analyzed by DLS. In some cases, the SV and antibody peaks were also analyzed by EM and DyMIN STED. The SV peak displayed small round profiles in the EM typical of synaptic vesicles, which was lacking in the antibody peak (Figure S2). DyMIN STED, as expected, detected fluorescence puncta in both peaks (Figure S2). DLS count was taken as a substitute for SV concentration, which allowed us to use the same amount of SVs (1000 counts/s) for immobilization on glass bottom dishes (Mat Tek, P35G-1.5-14-C) by incubating at 4°C for 1 h. Afterwards, SVs were fixed using 4% paraformaldehyde (Thermo scientific, 28908) in PBS (v/v) for 5 min and washed thrice in PBS at an interval of 5 minutes. If secondary antibody labeling was needed, the immobilized SVs were incubated in blocking solution for 30 minutes followed by secondary antibody incubation at a concentration of 8μg/ml (a dilution of 1:250) for 1 h at RT. Afterwards, samples were washed thrice with PBS at an interval of 5 minutes. Finally, mounting media (Invitrogen P36961) was applied on top of SVs and images were typically acquired within 48 h of sample preparation.

For two-color imaging in purified SVs, both mouse and rabbit antibodies of vesicular transporters were used except for VMAT2 and VAChT, for which only rabbit antibodies were used. To determine the proportion of SVs containing a specific transporter (Figure 2D), rabbit or mouse Syp antibody was used. Swapping the antibody species between Syp and respective transporters did not change the outcome. In some experiments where usage of the same species antibodies were required, secondary nanobodies were premixed with primary antibodies and used (multiplexing). VMAT2 and VAChT staining using multiplexing did not result in reproducible results and was not included in the analysis. The total number of analyzed vesicles (n) in the colocalization experiments (Figures 2C–2J) was more than 20,000 (20K) for VGLUT1, n>12K for VGLUT2, n>3K for VGLUT3, n>10K for VGAT, n>3K for VMAT2, n>3K for VAChT and n>20K for ZnT3.

DyMIN STED imaging

DyMIN STED nanoscopy was performed using a quad scanning STED microscope (Abberior Instruments, Göttingen, Germany) equipped with a UPlanSApo 100×/1.40 NA oil immersion objective (Olympus, Tokyo, Japan) and the optical set-up was described earlier (Heine et al., 2017). The pinhole was set to 1.0 Airy units and a pixel size of 15 nm was used. In two-color DyMIN STED imaging, Abberior Star Red (Ab.St.RED) and Alexa Flour 594 (AF594) combination was used while Alexa Fluor 488 (AF488), if required, was used as a reference marker in confocal mode. Ab.St.RED was excited at 640 nm and AlexaFluor 594 was excited at 561 nm while STED was performed at 775 nm wavelength. The fluorescence signal was detected using avalanche photo diodes with bandpass filters and a gating of 0.75–8 ns was applied. Pixel dwell times of 10-20 μs were used. Each line was scanned 3 times and the signal was accumulated. The typical image size for purified SVs was 50 μm^2. The number of images per transporter pair ranged from 10 to 50 per experiment. In comparisons between DyMIN and conventional STED and confocal acquisitions shown in Figure 1, the same excitation power for confocal and STED was used. The STED power in conventional STED corresponded to P_{max} of DyMIN STED (final step).

Colocalization analysis

To determine positive vesicular colocalization in DyMIN STED fluorescence images, we tagged epitope pairs that are known to be colocalized, using two spectrally distinct dyes and calculated the nearest neighbor distance (NND) of all the puncta in one channel

with respect to the other. As expected, the distribution of the NND values followed a Rayleigh distribution, as described earlier (Geumann et al., 2008). For example, we labeled two different epitopes of the same protein, Syp, with two distinct colors using a mouse (clone 72.1) and a rabbit Syp (clone G95) antibodies and calculated NND (Figures S4E–S4G). Although the corresponding images looked like mirror images of each other, we obtained a NND distribution with a median of approximately 15 nm.

Next, we performed a similar task but targeting two different proteins, Syp and Syb2, that was shown to be expressed in all SVs (Figures S4I and S4J) and again calculated NND for all spots. Since Syp and Syb2 are the two most abundant proteins by copy number (Wilhelm et al., 2014), we supposed that the fluorescent spots would be larger for both channels and thus yielding a larger NND distribution (median ~25 nm). The above two positive controls provided a realistic range for inter spot distances when the proteins of interest are closest (NND <30 nm; two epitopes on the same protein) or farthest (NND <50 nm; Syp and Syb2) on the same vesicle. From the above experiment, we adopted that any two proteins will be considered as colocalized on the same vesicle if the NND between the coordinates is less than 50 nm.

For colocalization analysis, the two-color images are median filtered using a radius of one pixel (15 nm) to remove single pixel background. Then, the coordinates of individual SVs in the two images were extracted simultaneously using ThunderSTORM, an open source plug-in for Fiji (Ovesny et al., 2014; Schneider et al., 2012). Using a custom written R script, the distance d between two puncta with coordinates (x_1, y_1) and (x_2, y_2) in the paired images was calculated using the formula,

$$d = \sqrt{(x_2 - x_1)^2 + (y_2 - y_1)^2}.$$

For colocalization analysis in culture neurons (Figure S6E), images were background subtracted using Rolling ball method with a radius of 50 pixels and colocalization correlation was performed using Coloc 2 plugin in Fiji. Costes' test (p=1) was repeated 100 times to test statistical significance of the determined colocalization coefficients.

Neuronal Cell Culture and Immunolabeling

Cultures of hippocampal neurons were prepared from Wistar rats at postnatal day P0–P1 using standard procedures (Kaech and Banker, 2006). For immunostainings, cells (16-22 DIV) were washed with PBS and fixed in 4% PFA in PBS (pH 7.4) for 20 min at RT, quenched with ammonium chloride and glycine (100 mM each) for 5 min, permeabilized with 0.1% Triton X-100 for another 5 min, and blocked in PBS supplemented with 1% BSA for 30 min. Both the primary and secondary antibody incubations were performed in PBS for 1 h at room temperature. Samples were mounted in ProLong Diamond Antifade Mountant medium (Thermo Fisher, P36961).

MINSTED DNA PAINT

Cultured hippocampal neurons, fixed (4% PFA for 10 min), quenched (100 mM NH4Cl2 for 10 min), permeabilized (5% TritonX-100 for 5 min) and blocked (5% NGS for 1 h), was indirectly immunolabeled against VGLUT1, ZnT3 and Piccolo (135308, 197011, SySy, 1:200 dilution) and Piccolo (142104, SySy, 1:500 dilution). The anti-mouse and anti-rabbit secondary antibodies were coupled to P1 and P3 docking strands at the 5' end (5'-3', P1 - TTA TAC ATC TA; P3 - TTT CTT CAT TA; Massive Photonics, 1:100 dilution). The imager strands contained Cy3B at the 3' end (5'-3', P1- CTA GAT GTA T; P3 - GTA ATG AAG A),) and the anti-guinea pig antibody was coupled to AF488 (1:500 dilution). The sample was post-fixed using 4% PFA following a washing step.

MINSTED nanoscopy enables an enhanced resolution by localizing single emitters with an effective STED PSF of FWHM d (Weber et al., 2021). Thus, the information from all emitted photons N can be used in order to find the emitter's position to an uncertainty σ scaling with $d/\sqrt{N}$, leading to further downsizing of STED resolution to the molecular scale. To achieve stochastic on/off switching of emitters, we performed DNA PAINT (Schnitzbauer et al., 2017) by labeling VGLUT1 and ZnT3, each with a specific ssDNA oligo (docking strand), through indirect immunolabeling. The transient binding of a complementary strand coupled to a fluorescent label (imager strand) in the imaging buffer was harnessed to capture stochastic fluorescence emission. The Piccolo signal marked the active zone (AZ) and was acquired in confocal mode in a large field of view followed by two-color MINSTED imaging in selected synaptic regions. Multiplexing was performed by sequential image acquisition with two different imager strands containing distinct oligo sequences (Schnitzbauer et al., 2017). Overall, the MINSTED-PAINT combination kept the background fluorescence low while achieving a localization precision of fluorophores below 1.5 nm within a maximum duration of 200 ms per localization in the focal plane. MINSTED measurements were carried out in PBS buffer containing the respective imager strand (5 nM) and $MgCl_2$ (75 mM). Initially, the piccolo signal (AF488) was acquired in confocal mode in a large field of view and a synaptic region of interest was selected for two-color MINSTED imaging. Multiplexing was performed by sequential image acquisition with two different imager strand solutions containing P1 or P3 sequences (Schnitzbauer et al., 2017).

For image analysis, the AZ centers were defined from the Piccolo confocal images as local maxima with a minimum prominence of 30% with respect to the global maximum. The localizations from two-color MINSTED images were filtered (27% of the localization events were discarded) and were subsequently clustered. Cluster analysis was performed by initially segmenting regions of high localization density using an in-house developed tessellation algorithm (Levet et al., 2015). The triangles of a Delaunay triangulation of all localizations $\vec{P}_i$ were assigned to segments if the triangles' corners were attributed a localization density D_i greater than the average localization density in the image and the triangles' edges were shorter than 20 nm. The localization density D_i at the corner $\vec{P}_i$ was estimated by C_i/A_i, where C_i is the number of unique corners and A_i the combined area of the triangles attached to $\vec{P}_i$. Non-assigned localizations were subsequently added to their closest segment if not further away than 30 nm with respect to the segment's

boundary. After discarding those segments with $\leq$ 10 localizations, a total of 863 and 504 clusters were found in the composite images of VGLUT1-ZnT3 (Figures 5I–5L) and in the VGLUT1-only (Figures 5D–5H) images, respectively. For two-color clustering, all localizations of both colors were merged and the clustering was performed "color blind", in order to be unbiased of the size of SVs. Identification of the colors of the assigned localizations following the clustering allowed quantification of VGLUT1 and ZnT3 co-localization in each cluster. Colocalization was not significantly different if clustering was performed separately for VGLUT1 and ZnT3 channels (data not shown). Both, VGLUT1-ZnT3 and VGLUT1-only clustering were based on the same dataset. In total, 22 two-color MINSTED images and 59 AZs from four different experiments were analyzed.

Copy number measurement

Isolated SVs from rat brain were labeled either for VGLUT1 or for ZnT3 using primary monoclonal antibody and secondary nanobody (Sograte-Idrissi et al., 2020) conjugated to a definite number of fluorophores resulting in a fixed stoichiometry between the number of protein molecules and fluorophores. Following single vesicle imaging, the copy number was obtained by dividing the SV fluorescence signal with the mean signal of the free antibody-nanobody complex (Figures 4E and 4F). SVs were labeled using monoclonal primary antibody (VGLUT1 – synaptic systems, Cat. No. 135011; ZnT3 synaptic systems, Cat. No. 197011) and secondary nanobody directed against the kappa light chain of mouse IgG (FluoTag®-X2, NanoTag Biotechnologies, Germany, Cat. No. N1202). Two fluorophores (Star RED, Abberior) are site-specifically coupled to one nanobody molecule ensuring a fixed stoichiometry of 4 to 1 (two nanobodies bind to each F(ab) of IgG molecule) for the number of fluorophores per IgG (Shaw et al., 2019; Sograte-Idrissi et al., 2020). Initially, 2.5-fold excess of secondary nanobody was added to the monoclonal primary antibody to saturate available binding sites of IgG. Then, the antibody-nanobody mixture was diluted 5 times using PBS and incubated for 1 h at RT with subtle shaking. The pre-incubated antibody-nanobody complex was diluted using blocking solution to reach concentrations optimized for the primary antibody and incubated with SVs with constant rotation for 1 h at RT. The labeled SVs were purified using SEC as described earlier, followed by immobilization and imaging. For the calculation of copy number, the fluorescence intensity of each vesicle puncta was divided by the mean fluorescence intensity of puncta corresponding to free antibody-nanobody complexes.

Immunoisolation

Immunoisolation of SVs was performed using paramagnetic Dynabeads (Takamori et al., 2000; Zander et al., 2010). 50 μl of Protein G Dynabead slurry was used per reaction. After washing the beads with 1 ml PBS (pH 7.4) three times with an interval of 10 min, ZnT3 antibody was added at a concentration of 24 μg/ml and incubated for 1h at 4°C with constant rotation. The antibody-beads mixture was washed once with PBS for 15min. This mixture was then incubated with 50 μg of LS1 protein overnight at 4°C under constant rotation. Next day, LS1-protein-dynabead mixture was washed thrice with an interval of 15 min each, using 1xPBS supplemented with protease inhibitors. Beads were transferred into new low binding Eppendorf tubes and spun down, placed on a magnet to completely remove the buffer from the beads. Afterwards, 50 μl of 5xLSB containing 10% Beta-mercaptoethanol was added to the bead pellet and the sample was subjected to heating at 70°C for 10 min with 750-800 rpm stirring. The vesicle concentration curve was run by increasing protein amount of LS1 with respect to IPs of ZnT3 and Syb2 (Schagger, 2006).

Quantitative immunoblotting

Determination of the amount of ZnT3 in SVs was performed using quantitative western blotting of SV proteins (CPG-SVs) in comparison to a standard curve of a highly purified full-length recombinant protein (Takamori et al., 2006). Increasing amount of SV and recombinant protein samples were loaded in the same gel and all measurements within the linear range of the standard curve were taken into account. Protein bands were visualized using an Odyssey CLx scanner (Li-cor) and signal intensities were analyzed using Fiji.

Glutamate uptake assay

LP2 fractions of SVs were prepared according to the protocol described previously (Takamori et al., 2006) from adult (5-8 weeks old) WT and ZnT3 KO mice brains. WT and KO LP2 samples for all glutamate uptake assays were prepared together to avoid differences in specimen quality. 15 μg of SVs was added to 90 μl of uptake buffer (300 mM Glycine, 10 mM MOPS-KOH, 2 mM MgSO4, pH 7.3) and incubated with 10 μl of 10X ATP-glutamate mix (10 mM potassium glutamate, 4 mM MgATP, 4 mM KCl) in a microtiter plate at 37°C for 15 minutes in the presence or absence of proton ionophore, 30 μM FCCP, and high affinity Zn^{2+} chelator, TPEN. 10X ATP-glutamate mix was adjusted accordingly for the uptake assays in the presence of Zn^{2+}. After 15 min, 90 μl of sample was transferred in a microfilter plate (MultiScreenHTS + HiFlow FB Filter Plate, Merck Millipore) and filtered using vacuum manifold while being washed thrice with 200 μl ice cold uptake buffer. In order to rupture SVs and measure fluorescence change, 50 μl iGluSnFR solution (1 μM purified iGluSnFR protein, 0.1% Triton X-100 resuspended in uptake buffer) was added per well and incubated for 30 min with gentle shaking at RT, protected from light. Fluorescence was measured using microtiter plate reader at excitation and emission wavelengths of 495 nm and 520 nm, respectively. The data were corrected for uptake in the presence of FCCP and normalized to the TPEN condition.Solutions with different Zn^{2+} concentrations were prepared using $ZnSO_4$ in different metal buffering systems (Qin et al., 2011; Vinkenborg et al., 2009).

For obtaining iGluSnFR standard curve, different glutamate concentrations ranging from 0 to 10 mM was added to uptake buffer (300mM Glycine, 10mM MOPS-KOH, 2mM MgSO4, pH 7.3) to make a final volume of 100 μl. The mixture was incubated in a microtitre plate at 37°C for 15 minutes. Afterwards, 50 μl iGluSnFR solution (1μM purified iGluSnFR protein, 0.1 % Triton X-100

resuspended in uptake buffer) was added per well and incubated for 30 min with gentle shaking at RT, protected from light. Later, the flourescence was measured using a microtitre plate reader at excitation and emission wavelengths of 495 nm and 520 nm respectively. Plasmid containing His6-tagged iGluSnFR variant, SF-iGluSnFR.A184S (Marvin et al., 2018), was kindly provided by L. Looger and purified by Ni-NTA affinity chromatography (Marvin et al., 2013).

Hippocampal slice preparation

WT (C57BL6/J) and ZnT3 KO mice (P19–P27, either sex) were anesthetized by diethylether and decapitated immediately. The brains were quickly removed, and horizontally sliced (400 μm) in ice-cold cutting buffer using a VT1200S vibratome (Leica). The cutting buffer composition (composition in mM): 26 $NaHCO_3$, 1.25 NaH_2PO_4, 4 KCl, 10 glucose, 230 sucrose, 0.5 $CaCl_2$, and 10 $MgSO_4$ (pH 7.4, osmolarity ~305 mOsm/L; equilibrated with 95% O_2 and 5% CO_2). The brain slices were then transferred to a custom-made holding chamber containing the ACSF solution and incubated at 37°C for at least 30 min, and further recovered at room temperature for more than 1 h before recording. ACSF solution (composition in mM): 125 NaCl, 26 $NaHCO_3$, 2.5 KCl, 1.25 NaH_2PO_4, 1 $MgCl_2$, 2 $CaCl_2$, and 25 glucose (pH 7.4, osmolarity ~305 mOsm/L; equilibrated with 95% O_2 and 5% CO_2). All experiments complied with national animal care guidelines, and were approved by the University Medical Center Göttingen board for animal welfare and the animal welfare office of the state of Lower Saxony.

Electrophysiology

Glass patch pipettes were pulled from borosilicate glass using a GB150TF-10 (Science Products) and had resistance of 2–5 MΩ. Brain slices were placed in the custom-made recording chamber kept at 37°C and were continually perfused with oxygenated ACSF (rate: 2.5ml/min). 10 μM bicuculine methiodide, 50 μM DAP-5 and 1 μM tetrodotoxin (TTX) were added to ACSF during the recordings. Cells were examined in a whole cell configuration under voltage clamp mode at a holding potential of -70 mV. Recordings were made using a custom-assembled rig including a microscope (Zeiss), a Patchstar 360 micromanipulator (Scientifica), a PPS2 perfusion system (Multichannel system) in a Faraday cage, and a HEKA EPC10 amplifier. Data were acquired with Patchmaster software (HEKA) at an acquisition rate of 20 kHz, and low-pass filtered at 2 kHz. During recordings, glass pipettes were filled with an internal solution (composition in mM): 130 $CsMeSO_4$, 5 TEA-Cl, 5 NaCl, 10 HEPES, 4 $MgCl_2$, 0.1 EGTA, 10 Na-creatinephosphate, 4 ATP and 0.4 GTP, pH 7.35, osmolarity ~300 mOsm/L. Zn^{2+} application is achieved by 5 min perfusion of ACSF containing 200 μM $ZnCl_2$. Uncompensated series resistance (*Rs*) was monitored by the delivery of 5 mV voltage step at defined points during the recording. Recordings were stopped or excluded if the *Rs* exceeded 20 MΩ, or changed by more than 20%. Events were analyzed by a custom-written macro in Igor Pro 6.36 software, as previously described (Clements and Bekkers, 1997).

Single cell transcriptome analysis

Raw expression values for each gene in each cell were normalized to the highest expression gene of the eight transporters to compare them across all cells. The gene expression levels are assigned between 0 and 1, where 1 means highest expression of the gene in that cell. If two genes had exactly the same expression in the same cell, both of these were assigned a value of 1. We clustered the co-expressed genes inside different cell types to generate a heat map. For cluster analysis, we used the Euclidean method as a clustering distance and default hierarchical clustering method in complex Heatmap R package version 2.5.4. To define cell types, we considered a gene expressed in a cell type if its normalized expression is more than 0.5 (meaning that its expression is more than half of the most expressed gene in that cell type). After obtaining the expression of unique genes expressed in each cell type, we quantified cell types that exhibited expression of more than one of the eight transporter genes.

Sample preparation for mass spectrometry

Purified synaptic vesicles were lysed using an equal volume of the lysis buffer (4% (wt/v) SDS, 100 mM HEPES, 1 mM EDTA in water), sonicated for 10 min using 30 s on/30 s off cycles at the maximum output of Bioruptor ultrasonication device (Diagenode, Seraing, Belgium). Protein concentration was assessed using BCA assay kit (Thermo Fisher Scientific, Bleiswijk, Netherlands) according to manufacturer's instructions. Cysteine moieties were reduced and alkylated using 10 mM tris(2-carboxyethyl)phosphine (TCEP) and 40 mM chloroacetamide (CAA) at 37 °C for 30 min. UPS2 standard (Sigma-Aldrich, Taufkirchen, Germany) was reconstituted in the lysis buffer and cysteines were reduced and alkylated as described above. 1.5 μg of UPS2 proteins were spiked into 9 μg of SV sample. Additionally, 1.5 μg of UPS2 standard without SV proteins and 9 μg of SV proteins without UPS2 standard were prepared. Proteins were purified using magnetic beads with carboxylate modified hydrophilic and hydrophobic surface (GE Healthcare, Buckinghamshire, UK) as described in (Hughes et al., 2019). Proteins were pre-digested in 50 mM ammonium bicarbonate buffer for 2 h at 37°C using recombinant LysC-protease (Promega, Madison, USA) at 1:100 LysC-to protein wt/wt ratio followed by the overnight digestion at 37°C using MS-grade trypsin (Promega, Madison, USA) at 1:20 trypsin-to-protein wt/wt ratio. Peptides were dried in a centrifugal Savant SpeedVac vacuum concentrator (Thermo Fisher Scientific, Waltham, USA), reconstituted in 2% (v/v) acetonitrile (ACN), 0.1% (v/v) trifluoroacetic acid (TFA) in water and subjected to LC-MS/MS analysis.

LC-MS/MS

Digested protein samples were analyzed in technical (injection) duplicates (SV samples with or without UPS2 proteins) or as a single injection (UPS2 proteins only) on a hybrid quadrupole-ion trap-orbitrap instrument (Orbitrap Fusion, Thermo Fisher Scientific, San

Jose, USA) using data-dependent (DDA) and data independent (DIA) acquisition methods. Peptides were concentrated onto a C18 PepMap100-trapping column (0.3 mm × 5 mm, 5 μm, Thermo Fisher Scientific, Waltham, USA) connected to an in-house packed C18 analytical column (75 μm ×300 mm; Reprosil-Pur 120 C18-AQ, 1.9 μm, Dr. Maisch GmbH, Ammerbuch, Germany). Liquid chromatography was operated on an UltiMate-3000 UHPLC nanosystem (Thermo Fisher Scientific, Waltham, USA). The columns were pre-equilibrated using a mixture of 95% buffer A (0.1% (v/v) formic acid (FA) in water) 5% buffer B (80% (v/v) ACN, 0.1% (v/v) FA in water). Peptides were eluted using a 118 min linear gradient from 5 to 7% buffer B over 3 min, from 7 to 20% over the next 57 min, from 20 to 32% over 30 min, and from 32 to 50% over 16 min. Elution was followed by a washing step at 90% buffer B over 6 min and a re-equilibration step at 5% buffer B over 6 min. MS was operated in DDA mode with the following settings: MS1 scans of 350-1650 *m/z* range were acquired in positive mode at the resolution of 120000 at 200 *m/z*, 300% automated gain control target (AGC), and 50 ms maximum injection time (IT). Most abundant peptide ions (charge states 2-7) were selected for MS/MS using an isolation window of 1.6 *m/z*. Peptide fragments were generated in an HCD cell at 28% normalized collision energy (NCE) and measured in Orbitrap at the resolution of 15000 at 200 *m/z*, normalized AGC of 1000%, and maximum IT of 54 ms. The duty cycle was kept at 2.5 s and dynamic exclusion at 30 s. When operated in DIA mode, MS1 spectra were acquired as in the DDA mode. Each MS1 scan was followed by 40 MS/MS scans of variable isolation window width. Peptide fragments were generated in an HCD cell at 30% NCE and measured in Orbitrap at the resolution of 30000 at 200 *m/z* and maximum IT of 54 ms.

LC-MS/MS data analysis

Raw MS data were analyzed using Spectronaut software ((Bruderer et al., 2015), v. 14.3.200701.47784). For each of the 2 biological replicates, a separate spectral library was built that included all DDA and DIA data from a given SV-replicate and the pure UPS2 standard protein. Spectral libraries were generated using a built-in Pulsar search engine under default settings. Specifically, *Rattus norvegicus* protein sequence database containing 29951 entries and retrieved from Uniprot (UniProt Consortium, 2019) in February 2019 was used in conjunction with UPS2 protein sequences (48 entries). Carbamidomethylation of cysteines was set as a fixed modification, and N-terminal protein acetylation and oxidation of methionine as variable modifications. DIA-based quantification was performed separately for each biological replicate using the respective spectral library. The settings were kept default except ''Q value sparse'' with no imputation and no cross-run normalization were selected for data filtering. iBAQ values (Schwanhäusser et al., 2011) were reported as protein group intensity values. The data was further analyzed using a custom R script. In brief, only proteins quantified with at least two peptides were retained in the data set. Decoy sequences, keratins, immunoglobulins, and trypsin were removed from the data. iBAQ intensities from the two technical replicates were averaged. Background-level intensities of proteins present in the UPS2 standard but identified in the SV sample without spiked-in UPS2 proteins were subtracted from UPS2 protein intensities in the SV sample containing spiked-in UPS2 standard. Additionally, iBAQ intensities were corrected by the protein sequence coverage and the protein concentrations were assessed using a linear model that was derived from the known protein amount of UPS2 proteins *vs.* iBAQ intensities in the first technical replicate ($R^2 = 0.614$). Only proteins quantified in both biological replicates are reported. If not specified otherwise, uncertainty in the protein concentration estimation is given as 68% confidence interval based on the fitted linear model. All raw mass spectrometry and software analysis files were deposited to the ProteomeXchange Consortium (www.proteomexchange.org) via the PRIDE (Perez-Riverol et al., 2019) partner repository. The variable window setup for DIA acquisition is provided in the supplemental information.

QUANTIFICATION AND STATISTICAL ANALYSIS

For single vesicle colocalization between two images, an 'object based' analysis was performed, implemented in R. Thus, the colocalization quantification is based on the actual number vesicles and not pixel correlation between the two channels analyzed. The method does not assume that the fluorescent intensity profiles between the two channels are comparable, which is appropriate for single vesicle analysis. Thus, composite or merged pseudo color images, as regularly used for 'pixel based' analysis, were avoided in the related figures (Figures 1, 2, S5, and S6). For colocalization analysis of confocal images in culture neurons (Figure S6E), a pixel based colocalization correlation was performed using Coloc2 plugin in Fiji. Costes' test (p=1) was repeated 100 times to test statistical significance of the determined colocalization coefficients. Statistical analysis for all experiments was performed using OriginPro 2020. In all experiments, statistical significance between two different samples was performed using unpaired t-test following confirmation of normal distribution of data sets (Figures 1B–1E, 4F, and 7D). This includes comparison of microscopy techniques in single vesicle imaging (Figures 1B and 1C), comparison of conventional and 'in-solution' labeling of purified vesicles (Figures 1D and 1E), comparison of copy numbers of VGLUT1 and ZnT3 samples (Figure 4F) and electrophysiological experiments (Figure 7D). The statistical significance of glutamate uptakes (nine samples) in the presence of different zinc concentrations was performed using two-way ANOVA (Figure 6B). The quantification in Figure 3 is based on the colocalization degree of each VT pairs and the respective proportion of each VT in the entire total SV population shown in Figure 2. Samples sizes of vesicles in the colocalization analysis is provided in both, STAR Methods and Figure legends.